www.sciencemag.org/content/360/6395/1326/suppl/DC1

Supplementary Materials for

Orientation-dependent stereo Wigner time delay and electron localization in a small molecule

J. Vos*, L. Cattaneo, S. Patchkovskii, T. Zimmermann, C. Cirelli, M. Lucchini, A. Kheifets, A. S. Landsman, U. Keller

*Corresponding author. Email: jvos@phys.ethz.ch

Published 22 June 2018, *Science* **360**, 1326 (2018)
DOI: 10.1126/science.aao4731

This PDF file includes:

Materials and Methods

1.1 Experimental details

The output of a multi-pass titanium: sapphire amplifier system with an estimated pulse duration of 30 fs and central wavelength of 776 nm is split (80:20) to generate pump and probe beams. The pump beam is focused on an argon-filled gas cell for high harmonic generation (HHG). The attosecond pulse train (APT) extends from high-order harmonic (HH) 15 to 27 at central photon energy of 34 eV, see Fig. S1A. The probe beam is passed through a piezo-controlled delay stage, after which it is superimposed on the pump beam. The beams are then focused collinearly on a cold jet of CO-molecules (Pangas, >99.9997% purity) using a toroidal mirror. After (dissociative) photoionization in the interaction region, electrons and (fragment) ions are extracted by dc uniform electric fields superimposed with an uniform magnetic field and guided towards time- and position-sensitive detectors (*37*).

The Reconstruction of Attosecond Beating By Interference of Two-photon Transitions (RABBITT) technique (see Fig. S1A and S1B) gives access to the evolution of the molecular photoionization dynamics, whereas the Cold Target Recoil Ion Momentum Spectroscopy (COLTRIMS) detector allows for coincidence detection of (fragment) ions and electrons. With a 4π acceptance angle for both particles, an access to the full three-dimensional momentum distributions per event is obtained.

We examine photoelectrons emitted within a total opening angle of 120° relative to the laser polarization axis. In the same fashion, we select photoelectrons in coincidence with C^+-fragment ions (acceptance angle of 20°). We separate the photoelectrons stemming from recoil events parallel ($\beta_{//} = 0 - 20^\circ$ and $\beta_{//} = 160 - 180^\circ$) and perpendicular ($\beta_{\perp} = 70 - 110^\circ$) to the laser polarization axis, see Fig. S1C. The contributions can be further separated according to the kinetic energy profile of the ionic fragment, i.e. the Kinetic Energy Release (KER). The photoelectrons are divided in a low KER and high KER region as indicated in Figure 1B. The emission angle of the photoelectron within the recoil frame Θ (acceptance angle 90°) is determined and two photoelectron spectra as a function of pump-probe delay are obtained, showing the photoionization dynamics for electron wave packets escaping on the carbon-side and the oxygen-side of the molecule (Fig. S1D).

1.2 Reconstruction of attosecond beating by interference of two-photon transitions

Photoionization of the CO molecule is induced by single photon absorption of an extreme ultraviolet (XUV) photon (Fig. S1A blue arrows). Single photon transitions, corresponding to HHs of the fundamental laser frequency, appear in the photoelectron spectrum at electron energies displaced from the photon energy by the ionization potential (I_p) of the occupied state. In the RABBITT pump-probe technique, the probe beam, split from the HH generation beam, interrogates the outgoing photoelectron via additional transitions (Fig. S1A red arrows). At the temporal and spatial pump-probe overlap, absorption of an XUV-photon followed by the absorption of an IR-photon or the absorption an XUV-photon of higher order followed by the emission of an IR-photon, leads to the same photoelectron final state. This results in the oscillation of the so-called sideband (SB) signal as a function of the pump-probe delay τ due to the interference between these two pathways (Fig. S1B).

The molecular photoionization dynamics are encoded in the phase of the oscillating SB signal (*26*):

$$S \cong \cos(2\omega_{IR}\tau - \Delta\varphi_{tot}) \cong \cos(2\omega_{IR}\tau - \Delta\varphi_{XUV} - \Delta\varphi_{mol}) \quad (2)$$

where ω_{IR} is the driving IR field frequency.

The total phase, $\Delta\varphi_{tot}$, reflects the dynamical information of the escaping photoelectron, including the attochirp, $\Delta\varphi_{XUV}$, and a molecular specific phase term, $\Delta\varphi_{mol}$. The first term, the attochirp of the ionizing XUV pulse is caused by the intrinsic emission delays in HH generation process. The second term, instead, is characteristic for each individual system and can be described by the sum of the two terms $\Delta\varphi_{mol} = \Delta\varphi_W + \Delta\varphi_{CC}$, with $\Delta\varphi_{CC}$ being the measurement-induced phase term that stems from the continuum-continuum transition in the IR field (*32*). The target specific Wigner phase term, $\Delta\varphi_W$, is the term we want to access in order to extract the Wigner time delay difference according to: $\tau_W = \Delta\varphi_W/2\omega_{IR}$. The stereo-specific measurement is insensitive to contributions from additional phase terms apart from the target specific Wigner time delay. In particular, the attochirp contribution, $\Delta\varphi_{XUV}$, cancels out by comparing the phase terms of SB signals conceived by the same photon energies. Additionally, assuming that the ionization probability is slowly varying with energy, $\Delta\varphi_{CC}$ is removed due to the symmetric contribution of the long-range Coulomb potential (*32*). The stereo Wigner time is subsequently given by:

$$\tau_{SW} = \frac{\Delta\varphi_W(\text{carbon-side}) - \Delta\varphi_W(\text{oxygen-side})}{2\omega_{IR}} \quad (3)$$

thereby yielding the absolute difference in Wigner time delay within the molecular frame.

1.3 Data-analysis

The difference in time delays between the carbon-side (Fig. S2B) and the oxygen-side (Fig. S2C) of the molecule, defined as the stereo Wigner time delay τ_{SW}, are extracted from 8 independent measurements with an integration time of 3600 s per delay step. We separate the RABBITT traces according to the recoil angle of the ionic fragment and the emission angle Θ of the photoelectron with respect to the polarization axis, by that obtaining spectra referring to electrons escaping the binding potential on the oxygen-side or carbon-side of the geometric center of the molecule, see Fig. S2.

We select each sideband to be integrated over a specific energy range indicated by the horizontal bars in Fig. 3. The signal is Fourier transformed (Fig. S2F and S2G) and its projection is windowed (Fig. S2J and S2K) before it is converted back to the time-domain. The raw (square-solid thin line) and Fourier-filtered (solid thick line) sideband signals for each sideband are displayed in Fig. S2E and S2I), separated according to Θ_e (oxygen-side in red, carbon-side in grey in Fig. S2B and S2C).

The stereo Wigner time delays are shown for orientation- and KER- resolved photoionization channels (Fig. 3). The vertical error bar represents the uncertainty in the experimental results as a combined term of the statistical standard deviation over all measurements with each measurement independently weighted with the uncertainty of its sideband fit. Each error bar is given by:

$$\delta_W = \sqrt{\frac{N\sum_{i=1}^{N}\frac{(x_i-\bar{x}_W)^2}{\sigma_i^2}}{N-1\sum_{i=1}^{N}\frac{1}{\sigma_i^2}} + \left(\frac{\sum_{i=1}^{N}\frac{1}{\sigma_i}}{\sum_{i=1}^{N}\frac{1}{\sigma_i^2}}\right)^2}$$

where the weighted mean is given by

$$\text{------} = \frac{\sum_{i=1}^{N}\frac{x_i}{\sigma_i^2}}{\sum_{i=1}^{N}\frac{1}{\sigma_i^2}}$$

and the number of independent measurements is N (*3*). We would like to emphasize that this treatment of the error is rather an over-estimation than an under-estimation based solely on the statistical error.

2 Time-Dependent Resolution in Ionic States

2.1 Method

Electronic structure calculations for the CO molecule and its molecular cations used correlation-consistent valence triple-zeta basis set, augmented with diffuse functions (aug-cc-pVTZ) (*38*). The experimental geometry of the neutral ground state ($X^1\Sigma^+$, R_e=1.128323 Å (*39*)) was used. In order to improve accuracy and numerical stability of the grid-based calculations (see below), large-core [1s] scalar relativistic effective-core potential (*40*) (ECP) was used on both carbon and oxygen nuclei. We verified that the all-electron and ECP calculations lead to consistent results for the states of interest. Vertical excitation energies agree to better than 0.1 eV. Dyson orbital norms agree to better than 2% between the ECP and all-electron calculations.

One-particle orbitals were optimized using the full-valence complete active space self-consistent field (CASSCF) solution, optimized for the equally-weighted $1^2\Sigma^+$, $2^2\Sigma^+$, $3^2\Sigma^+$, $1^2\Pi_x$, $1^2\Pi_y$, $2^2\Pi_x$, $2^2\Pi_y$ states of CO^+. The same (9e,8o) CAS was previously used by (*23*). Electronic states of the cation and the neutral were calculated using multi-reference configuration-interaction singles (MR-CIS) approach, with all CASSCF determinants included in the reference space. We verified that the MR-CIS wavefunction of the neutral is essentially identical to the CAS(10,8) wavefunction optimized for the pure neutral state (wavefunction overlap of 0.996, total energy change 0.017 eV).

The MR-CIS approach is not size-consistent, and suffers from a slight imbalance in the treatment of dynamical correlation between the cation and the neutral species. To compensate for this defect, we have uniformly shifted the calculated energies of all cationic states upwards by 0.944 eV, to match the experimental vertical ionization potential (I_p) of carbon monoxide. The resulting doublet states of CO^+ are summarized in Table S1.

2.2 Orientation-dependent photoionization time delays

We calculate orientation-dependent ionization delays by performing a numerical experiment with time-dependent resolution in the ion states (TD-RIS) technique (*33, 34*).

The center of mass of the $^{12}C^{16}O$ molecule is placed at the origin of a simulation box, extending to 15.12 Bohr in the X,Y directions, and to 30.24 Bohr in the Z direction (Fig. S3C). A uniform, Cartesian-product grid has a spacing of 0.18 Bohr. An 8.19 Bohr wide transmission-free absorbing boundary (*41*) (k_{min}=0.8, δ=0.2) is applied on all edges. The Dyson and "cradle" orbitals, electron densities, transition density matrices, permanent and transition dipoles are calculated from the MR-CIS wavefunctions (*42*), for the 18 channels used in the simulation (Table S1).

We separately record the probability of an electron reaching the absorber on the positive- and negative-Z faces of the simulation volume, as a function of time (Fig. S3B). The probability is observed separately for each final state of the cation. Our 1:1:3 geometry of the simulation volume yields an electron acceptance angle of ~ 0.81 sterad, similar to a cone with an opening angle of 60 degree (acceptance angle of 30 degree).

The desired observables (see below) can be represented as integrals over the joint probability distribution of the molecular orientation and photoelectron direction at time *t*. In the molecular frame, where laser polarization direction is taken along the Z axis, this distribution can be expressed as an expansion over bipolar harmonics (*43*):

$$P(\hat{r}_m, \hat{r}_e, t) = \sum_{l_1,l_2,L,M} C_{l_1 l_2 LM}(t)\{Y_{l_1}(\hat{r}_m) \otimes Y_{l_2}(\hat{r}_e)\}_{LM} \quad \text{(S1)}$$

where $\hat{r}_m$ is the molecular axis direction and $\hat{r}_e$ is the direction in which photoelectron is detected. For a one-photon process, symmetry of the dipole interaction Hamiltonian requires that $P(\hat{r}_m, \hat{r}_e, t)$ is invariant to rotations around the Z axis and reflections in the σ_{xz} and σ_{xy} planes. As the result, coefficients $C_{l_1 l_2 LM}(t)$ vanish unless $l_1 + l_2$ is even, L is even, and *M* is zero.

In order to determine the non-zero coefficients $C_{l_1 l_2 LM}(t)$, we consider the following local orientations of the CO molecular axis:

- along the local Z axis
- in the XZ plane, $\pm$30, $\pm$60, and $\pm$90 degree from the Z axis
- in the YZ plane, $\pm$30, $\pm$60, and $\pm$90 degree from the Z axis

In all three cases, the oxygen end of the molecule is pointing towards positive local Z direction. Each case, the electric field polarization direction is chosen in the XZ plane, at 0, 30, 60, and 90 degree from the local Z axis. Due to the Hamiltonian symmetry, only 29 of these 52 geometries are unique and need to be calculated explicitly. In the molecular frame of reference, these geometries are illustrated in Fig. S4. These geometries are sufficient to uniquely determine $C_{l_1 l_2 LM}(t)$ with $l_1 \leq 4, l_2 \leq 4, L \leq 8$.

Due to the proximity of the absorber to the molecular ion, the detector arrival times need to be corrected for the asymmetry in the long-range interaction potential. Classically, the lowest-order correction is given by (atomic units):

$$\Delta t = \mp \frac{p_z}{v_0^3 R_0} \quad \text{(S2)}$$

where $p_z$is the Z component of the dipole moment, v_0 is the electron velocity at infinity, and R_0 is the starting position (here taken as the mid-point of the absorber). The - and + signs apply for the positive and negative local Z directions, respectively.

2.3 Detection geometry

In order to closely mimic the experimental detection geometries, we define the four observables, corresponding to distinct orientations of the molecular axis and photoelectron direction relative to the laser polarization axis. In terms of the joint probability function

$$
\begin{aligned}
&P_{1s}(t) \\
&= 2\pi \int_0^{\beta_{max}} d\theta_m \int_0^{\alpha_{max}} d\theta_e \int_0^{2\pi} d\phi_e [\sin\theta_m \sin\theta_e \, P(\hat{r}_m, \hat{r}_e, t) \Theta_s(\hat{r}_m, \hat{r}_e)] \\
&+ 2\pi \int_{\pi-\beta_{max}}^{\pi} d\theta_m \int_0^{\alpha_{max}} d\theta_e \int_0^{2\pi} d\phi_e [\sin\theta_m \sin\theta_e \, P(\hat{r}_m, \hat{r}_e, t) \Theta_s(\hat{r}_m, \hat{r}_e)] \\
&+ 2\pi \int_0^{\beta_{max}} d\theta_m \int_{\pi-\alpha_{max}}^{\pi} d\theta_e \int_0^{2\pi} d\phi_e [\sin\theta_m \sin\theta_e \, P(\hat{r}_m, \hat{r}_e, t) \Theta_s(\hat{r}_m, \hat{r}_e)] \\
&+ 2\pi \int_{\pi-\beta_{max}}^{\pi} d\theta_m \int_{\pi-\alpha_{max}}^{\pi} d\theta_e \int_0^{2\pi} d\phi_e [\sin\theta_m \sin\theta_e \, P(\hat{r}_m, \hat{r}_e, t) \Theta_s(\hat{r}_m, \hat{r}_e)] \quad \text{(S3)}
\end{aligned}
$$

$$
\begin{aligned}
&P_{1o}(t) \\
&= 2\pi \int_0^{\beta_{max}} d\theta_m \int_0^{\alpha_{max}} d\theta_e \int_0^{2\pi} d\phi_e [\sin\theta_m \sin\theta_e \, P(\hat{r}_m, \hat{r}_e, t) \Theta_o(\hat{r}_m, \hat{r}_e)] \\
&+ 2\pi \int_{\pi-\beta_{max}}^{\pi} d\theta_m \int_0^{\alpha_{max}} d\theta_e \int_0^{2\pi} d\phi_e [\sin\theta_m \sin\theta_e \, P(\hat{r}_m, \hat{r}_e, t) \Theta_o(\hat{r}_m, \hat{r}_e)] \\
&+ 2\pi \int_0^{\beta_{max}} d\theta_m \int_{\pi-\alpha_{max}}^{\pi} d\theta_e \int_0^{2\pi} d\phi_e [\sin\theta_m \sin\theta_e \, P(\hat{r}_m, \hat{r}_e, t) \Theta_o(\hat{r}_m, \hat{r}_e)] \\
&+ 2\pi \int_{\pi-\beta_{max}}^{\pi} d\theta_m \int_{\pi-\alpha_{max}}^{\pi} d\theta_e \int_0^{2\pi} d\phi_e [\sin\theta_m \sin\theta_e \, P(\hat{r}_m, \hat{r}_e, t) \Theta_o(\hat{r}_m, \hat{r}_e)] \quad \text{(S4)}
\end{aligned}
$$

$$
\begin{aligned}
&P_{2s}(t) \\
&= 2\pi \int_{\frac{\pi}{2}-\beta_{max}}^{\frac{\pi}{2}+\beta_{max}} d\theta_m \int_0^{\alpha_{max}} d\theta_e \int_0^{2\pi} d\phi_e [\sin\theta_m \sin\theta_e \, P(\hat{r}_m, \hat{r}_e, t) \Theta_s(\hat{r}_m, \hat{r}_e)] \\
&+ 2\pi \int_{\frac{\pi}{2}-\beta_{max}}^{\frac{\pi}{2}+\beta_{max}} d\theta_m \int_{\pi-\alpha_{max}}^{\pi} d\theta_e \int_0^{2\pi} d\phi_e [\sin\theta_m \sin\theta_e \, P(\hat{r}_m, \hat{r}_e, t) \Theta_s(\hat{r}_m, \hat{r}_e)] \quad \text{(S5)}
\end{aligned}
$$

$$
\begin{aligned}
&P_{2o}(t) \\
&= 2\pi \int_{\frac{\pi}{2}-\beta_{max}}^{\frac{\pi}{2}+\beta_{max}} d\theta_m \int_0^{\alpha_{max}} d\theta_e \int_0^{2\pi} d\phi_e [\sin\theta_m \sin\theta_e \, P(\hat{r}_m, \hat{r}_e, t) \Theta_o(\hat{r}_m, \hat{r}_e)] \\
&+ 2\pi \int_{\frac{\pi}{2}-\beta_{max}}^{\frac{\pi}{2}+\beta_{max}} d\theta_m \int_{\pi-\alpha_{max}}^{\pi} d\theta_e \int_0^{2\pi} d\phi_e [\sin\theta_m \sin\theta_e \, P(\hat{r}_m, \hat{r}_e, t) \Theta_o(\hat{r}_m, \hat{r}_e)] \quad \text{(S6)}
\end{aligned}
$$

where we already used the axial symmetry of the joint distribution to evaluate the integral over ϕ_m. The directions $\hat{r}_m$ and $\hat{r}_e$ are determined by the pairs of polar coordinates θ_m, ϕ_m and θ_e, ϕ_e respectively. Finally, functions Θ_s and Θ_o are defined in terms of the Heaviside function Θ:

$$\Theta_s(\hat{r}_m, \hat{r}_e) = \Theta(\theta_{max} - \arccos(\hat{r}_m \cdot \hat{r}_e)) \quad (S7)$$

$$\Theta_o(\hat{r}_m, \hat{r}_e) = \Theta(\theta_{max} - \arccos(\hat{r}_m \cdot \hat{r}_e)) \quad (S8)$$

The parameters β_{max}, α_{max}, and Θ_{max} are chosen as 20, 60 and 90 degree, respectively. The physical meaning of the observables $P_{1s} - P_{2o}$ is as follows:

- P_{1s} corresponds to the molecular axis oriented within β_{max} degrees and photoelectron departing within an α_{max} degrees from the laser polarization direction. The angle between the photoelectron departure direction and the oxygen end of the molecule does not exceed Θ_{max}.
- P_{1o} is similar to P_{1s}, except that the photoelectron departs within θ_{max} degrees from the carbon end of the molecule.
- P_{2s} and P_{2o} are similar to P_{1s} and P_{1o}, except that the molecular axis is oriented within β_{max} degrees from the plane normal to the laser polarization direction.

2.4 Experimental conditions

The XUV pulse used in experiment has a complex spectral and temporal structure. Because we are interested in a 1-photon ionization process, it is sufficient to consider the spectral components of the pulse separately. For each harmonic, we employ a truncated Gaussian pulse of 0.4 (1.0) fs full width half maximum (FWHM, baseline) duration and peak intensity of 1 TW cm^{-2}. The corresponding peak of the electric field intensity is F_0=5.345·10^{-3} a.u. (~0.275 V/Å). The central frequency of each pulse is chosen as an odd harmonic (N=15 ... 27) of the driving 771 nm laser field. The XUV attochirp is taken 23 as/eV. Each harmonic pulse has the fluence of ~ 2.71 mH/Bohr^2. We calculate the time delays for the carrier-envelope phase (CEP) ϕ=0 and π, and average the two results to eliminate direction bias due to the CEP. The parameters of the XUV pulses are summarized in Table S2.

The experimental measurement does not distinguish between the ion states with the same final fragmentation product. Given the large number of accessible electronic states (see Table S1) and the presence of several harmonic components in the XUV pulse, many ionization channels may contribute to the signal at a given photoelectron energy. To model the experimental direction-dependent time delays, we construct an incoherent weighted-average of the time vs. photoelectron yield curves. The pulse composition and the attochirp used for averaging are shown in Table S2.

2.5 Discussion

It is important to understand the limitations and possible sources of artifacts in our approach. In addition to the usual accuracy and convergence issues inherent in the underlying quantum-chemistry methods, the calculated yields and time delays in our simulations may also be affected by the presence of the Rydberg and autoionizing states. Rydberg states converging to all available ionization thresholds will be inevitably populated by the short, broad band harmonic pulses presently used (see Table S2). These states will decay after the pulse ends, creating a steady (if a single Rydberg state was populated) or oscillating (in case of the presence of a coherent wavepacket) exponential decay due to the overlap of the absorbing boundary and the Rydberg state. The

contribution from the Rydberg state decay will depend sensitively on the extent of the simulation volume.
Furthermore, all excited states of neutral CO associated with the 4Π and higher continua are autoionizing. Unless a state is of a Rydberg character as well, the time constant for autoionization will not depend on the simulation volume. Decay of these states will create a long electron emission tail, with their own time dependence and asymmetry parameters. Depending on the lifetime of each state, it may be impossible to cleanly separate the signal from the direct electrons.
Another potential source of inaccuracies is the calculated time delays is the truncation of the bipolar-harmonics expansion at finite, small l_1, l_2 and L values (Eq. S1). These values must be large enough to describe partial waves present in the photoelectron spectrum of an oriented molecule. This requirement becomes more stringent at low photoelectron energies. For example, restricting the fit to $l_1 \leq 3, l_2 \leq 3, L \leq 6$ (data not shown) decreases calculated time delays for the "parallel" observation geometry by 25-50%. In the "perpendicular" observation geometries, it causes a sign change in the time delays in the $D^2\Pi$ channel for photoelectron energies below 6 eV. It is possible that our present results (obtained with $l_1 \leq 4, l_2 \leq 4, L \leq 8$) may be further modified upon inclusion of higher angular momentum terms in the expansion.

2.6 Direction-dependent photoionization time delay

The calculated direction-dependent time delays for the individual final states of the molecular ion and individual harmonic pulses are summarized in Table S3. For some combinations of the ion state and ionizing harmonic, the ion-yield curves show a distinct, complex time behavior on the carbon- and oxygen-side detectors (see Fig. S5a), precluding determination of differential arrival times, or produce very large apparent photoelectron delays (see Fig S5b). This behavior is seen for low photoelectron energies and final states with high angular momentum.
From Table S3 it is clear that the photoelectron signal at a given energy may originate from ionization events leaving several different states. Final-state resolution is therefore desirable for obtaining a clean measurement. In the experiment, the photoelectron signal was not final-state resolved. To illustrate the time delays expected in this case, we construct a simulated photoelectron and time-delay spectrum, using a pulse with spectral composition given in Table S2.
The simulated photoelectron spectra associated with the stable or metastable CO^+ molecular ions are shown in Figs. S6a and S6b.
The photoelectron spectrum associated with the $C^+ + O$ fragmentation channel are shown in Fig. S7a and S7b.

3 Classical Wigner Propagation Method (CWP) and nonadiabatic nuclear dynamics simulations

3.1 CWP Method

The XUV pulse used in the streaking or RABBITT experiments is relatively weak justifying the use of the first-order perturbation theory to describe the interaction with the XUV field. Within the perturbation theory the wave function $\psi(t)$ may be written as

$$\psi(t) = \psi^{(0)}(t) + \psi^{(1)}(t)$$
$$= U_0(t - t_0)\psi^{(0)}(t_0)$$
$$- \frac{i}{\hbar}\int_{t_0}^{t} U_0(t - t')H_{XUV}U_0(t' - t_0)\psi^{(0)}(t_0)dt' \quad \text{(S9)}$$

where $H_{XUV}(t) = -\vec{\mu}_e\vec{E}_{XUV}(t)$, $\vec{\mu}_e = eq$ is the dipole operator, $\vec{E}_{XUV}(t) = \vec{\epsilon}E_{env}(t)\cos(\omega_c t)$ is the XUV field in the dipole approximation, and $U_0(t) = e^{\frac{-iH_0(t)}{\hbar}}$ is the propagator with the Hamiltonian H_0 of the molecule in the field of the IR probe.
The first step in evaluation of the integral in Eq. (S9) from right to left is the propagation with $U_0(t' - t_0)$. Neglecting the polarization of the molecule due to the IR field, the propagation simply adds the phase factor $e^{iE_0(t'-t_0)/\hbar}$, where E_0 is the ground-state energy. In the second step, the wave-function $\psi^{(0)}(t')$ is ionized with $H_{XUV}(t')$ giving $\psi_{XUV}(t') = H_{XUV}(t')\psi^{(0)}(t')$. In the third step, $\psi_{XUV}(t')$ is propagated with $U_0(t - t')$. In the typical RABBITT or streaking experiment, the spectrum of $\psi_{XUV}(t')$ is almost exclusively in the continuum part, above the ionization threshold. Exploiting the fact that propagation of continuum states is often close to the classical limit, $\psi_{XUV}(t')$ is transformed into the Wigner phase-space representation and propagated with the classical Wigner method (*44, 45*).
The Wigner transformation of the integral containing $\psi_{XUV}(t')$ is two dimensional in time. It contains "off-diagonal" terms corresponding to Wigner functions with $\psi_{XUV}(t')$ and $\psi^*_{XUV}(t'')$, where $t' \neq t''$. These terms are together with the fast-oscillating carrier wave of the XUV pump pulse responsible for the resolution of the energy spectrum of the pump pulse. Indeed, analytic solution of the perturbation-theory integral in terms of eigenstates of H_0 shows that $\psi^{(1)}$ for the δ-pulse and a pulse of a finite length differ only by $\tilde{E}^2_{pulse}(E)$, which is the finite-length pulse in the frequency domain. In analogy, the two-dimensional time integral can be approximately reduced to a single-dimensional integral by using only the diagonal terms where $t' = t''$ (as with the δ-pulse) and the energy-resolved Wigner transform of $\psi_{XUVe}(t')$

$$W_{XUVe}(q,p,t) = \tilde{E}^2_{XUV}(H_0(q,p) - E_0)\int d^D\xi\, \psi_{XUVe}\left(q + \frac{\xi}{2}, t'\right)\psi^*_{XUVe}\left(q + \frac{\xi}{2}, t'\right)e^{i\xi.\frac{p}{\hbar}} \quad \text{(S10)}$$

where $H_0(q,p)$ is the Wigner transform of H_0 and $\tilde{E}^2_{XUV}(E)$ is the XUV pump in the frequency domain.
In addition to computing the photoionization delays, the classical Wigner method is also used to compute the photoionization yields. It suffices to set the IR field to zero, the envelope of the XUV pulse $E_{env}(t) = \delta(t)$, and to analyze the energy dependence of the ionized part of $W_{XUVe}(q,p,t)$.

In the electronic structure calculations, the internuclear distance in the CO molecule was set to the experimental value of 1.128 Å (*46*). The multi-electron wave function was computed with the Gamess code (*47*) using the MR-CIS/aug-cc-pVTZ method based on the CASSCF(10,8) reference for the neutral CO and on the CASSCF(9,8) reference for CO^+. The single-active electron approximation was used to describe the ionization process with the initial wave-function of the ionizing electron computed as the Dyson orbital (DO) between the neutral CO and corresponding ionic state using the Superdyson

code (*48*). The electrostatic interaction of the ionized electron with the CO^+ ion was approximated by the multipole expansion up to the octupole level centered in the center of mass.
Eq. (S10) is used to obtain the initial conditions for the classical propagation (see Ref. (*49*) for details), which is done in the IR field with a peak strength of 0.008 au. In the framework of the scattering theory, it was shown that the delays obtained from the simulated streaking trace are the same as the delays extracted from the corresponding RABBITT scenario (*32, 50*). The continuum-continuum delay, τ_{CC}, which is responsible for the RABBITT sidebands, in fact, was demonstrated to be nearly identical to the Coulomb-laser coupling delays, τ_{CLC}, observed in the attosecond streaking technique (for a detailed discussion on the relationship between τ_{CC} and τ_{CLC}, see Ref. (*50*), section 4.3). The integration over different orientations of the CO axis with respect to the XUV-IR polarization axis was done using the trapezoidal rule with the steps of 10 degrees, taking into account the area of the corresponding solid angle. Similar to the experiment, in the parallel orientation, the angle between the CO axis and XUV-IR polarization axis ranged from 0 to 20 degrees. In the perpendicular orientation, the angle ranged from 70 to 110 degrees. The photo-electron detector acceptance angle was 60 degrees measured from the polarization axis.

3.2 Nuclear Dynamics

The dissociation of CO^+ was described using a one-dimensional model neglecting the effects of the rotational degrees of freedom. The initial nuclear wave-packet was obtained within the Condon approximation as the vibrational ground state of CO in the harmonic approximation. The potential energy surfaces (PES) and nonadiabatic coupling matrix elements (NACME) were computed with the Molpro code (*51*) at the MRCI/def2-TZVPP level of theory. The reference wave-function was computed with SA-CASSCF(9,8)/def2-TZVPP. For $^2\Sigma$ states the reference function was averaged over 7 lowest states of the $^2\Sigma$ symmetry. Eleven states were resolved with the MRCI method in the space of 17 reference states (which included also Δ states). For $^2\Pi$ states the reference function was averaged over six lowest states of $^2\Pi$ symmetry. Seven MRCI states were resolved using seven reference states. The NACME were computed numerically, using the three-point formula with the step of 0.01 a.u.. The PES and NACME for $^2\Sigma$ states are shown in Fig. S8, for $^2\Pi$ states in Fig. S9. For $^2\Sigma$ states, five potential energy surfaces were considered in the dynamics: $3^2\Sigma^+, 4^2\Sigma^+, 5^2\Sigma^+, 6^2\Sigma^+$, and $7^2\Sigma^+$. For $^2\Pi$ states, six potential energy surfaces were considered: $D^2\Pi, 3^2\Pi, 4^2\Pi, 5^2\Pi, 6^2\Pi$, and $7^2\Pi$. All $^2\Sigma$ states are in good agreement with the states published in (*23*), which were computed with a similar method, except for the discontinuity of the first derivative appearing in $6^2\Sigma^+$ of (*23*). Since $6^2\Sigma^+$ was the highest state considered in (*23*), the discontinuity can be attributed to a limited electronic space used in (*23*). $D^2\Pi$ and $3^2\Pi$ are in good agreement with those reported in (*23*), while for higher lying $^2\Pi$ states, the agreement is rather qualitative. The nuclear wave packets were propagated in the adiabatic basis using the second-order Fourier method (*52*).
Several dissociative $^2\Sigma$ and $^2\Pi$ states of CO^+ were considered when computing the photoionization delays: 1) four Σ states starting from the lowest dissociative state $3^2\Sigma^+$ and 2) seven lowest dissociative $^2\Pi$ states were initially computed, but only three states ($D^2\Pi, 3^2\Pi$ and $9^2\Pi$) corresponding to a DO with a norm higher than 0.0025 (which

is roughly $1/10^{\text{th}}$ of the lowest-norm $^2\Sigma$ orbital). Since the photoelectron yield is directly proportional to the norm of a DO, only those three $^2\Pi$ states were considered further. The ionization potentials (I_p) and norms of the corresponding DO (spectroscopic intensity factors (SIF)) are shown in Table S4. Considering the spectrum of the XUV experimental pulse, states with even higher I_p (than the highest I_p states considered in this work) can contribute to the experimental photoelectron spectrum, but only to the one and two lowest order side-bands in the measured RABBITT traces.

3.3 Orientation-dependent photoionization time delays

The energy-dependent stereo-photoionization delays in the parallel and perpendicular orientation of CO with respect to the XUV field are shown in Fig. S10. Several general observations can be made: $^2\Sigma$ states have negative delays (the only exception being $5^2\Sigma^+$ in the perpendicular orientation) whereas $^2\Pi$ states have positive delays. In addition, the stereo delays in the parallel orientation are higher in the absolute value than in the perpendicular orientation.

3.4 Detection geometry

The photoionization yields shown in Fig. S11 were computed using the same detection parameters used for the stereo-photoionization delays. The $3^2\Sigma^+$ state presenting the highest SIF also has the highest yield.

3.5 Dissociation dynamics

The mean rotational period of CO at 10 K (roughly corresponding to the experimental conditions) equals to 10.3 ps. This sets the limit for the dissociation into the orientation-resolved cone of 20° to ~1 ps after the ionization. KER spectra and dissociation fraction were therefore computed after propagating the nuclear wave packet for 1 ps from the ionization time. The KER spectra (shown in Fig. S12) were computed after discarding a part of the nuclear wave packet corresponding to the C-O bond distance shorter than 10 a.u.. The dissociation fraction (see Fig. S13) is computed in the same fashion as the norm of the wave-function corresponding to C-O bond distance greater than 10 a.u.. Each state was propagated individually. In accordance with higher electronegativity of oxygen, almost all states adiabatically dissociate towards the $C^+ + O$ limit, except for $4^2\Sigma^+$ and $6^2\Pi$ which dissociate towards the $C + O^+$ limit. Since only $C^+ + O$ was detected in the experiment, asymptotic populations dissociating on $4^2\Sigma^+$ and $6^2\Pi$ were ignored in the calculations of KER spectra and dissociation fractions.

The populations of electronic states during the dissociation process are shown in Fig. S14. While $3^2\Sigma^+$ dissociates essentially adiabatically, the dynamics of all other states is highly nonadiabatic.

The KER spectra of individual states are shown in Fig. S12. The KER spectra of $3^2\Sigma^+$ and $D^2\Pi$ are located between 0 to 2 eV, while the other states dissociate mostly at higher energies. The KER spectrum of $3^2\Sigma^+$ has a single dominating narrow peak due to tunneling involved in the dissociation. Relatively short time interval of 1 ps together with slow tunneling rate prevents peaks from lower vibrational states from appearing. Had the simulation time been much longer, lower lying peaks should have appeared (*31*). The spectrum of $D^2\Pi$, on the other hand, consists of many well resolved peaks due to

vibrational dynamics of the wave packet which involves several strongly coupled states (mainly $D^2\Pi$ and $3^2\Pi$). This is in agreement with earlier observations (*31*).
The spectrum of $3^2\Pi$ consists of a broad peak at around 5 eV accompanied by several sharp peaks. These are partly due to a quasi-bound state formed in the strongly coupled Franck-Condon region and partly due to the interference of dissociation pathways. Splitting of $3^2\Pi$ population between two main dissociation limits $L_1^{C^+}$ and $L_2^{C^+}$ agrees well with the experimental observation (*22*), even though the simulation seems to overestimate the relative intensity of $L_1^{C^+}$ in comparison with the experiment. On the other hand, the sharp peaks above ~2 eV are not visible in the KER spectrum measured in the current experiment in the perpendicular orientation, which should be dominated by the signal from $3^2\Pi$ above 2 eV. The spectrum of $4^2\Sigma^+$ consists mainly of two broad peaks and, again, the main features seem to be in agreement with experimental findings (*22*) including splitting between $L_2^{C^+}$, $L_4^{C^+}$ and $L_3^{C^+}$ with decreasing orders of importance. The only $C + O^+$ channel ($L_1^{O^+}$) represented in the calculation receives around 40% of the intensity. The experiment (*22*) shows that a fraction of $4^2\Sigma^+$ dissociates to higher O^+ dissociation limits, which adiabatically couple to high-lying $^2\Sigma$ states, not considered in the simulation. Therefore, the simulation might overestimate the fraction of $4^2\Sigma^+$ dissociating to $C^+ + O$ channel slightly. Finally, $5^2\Sigma^+$ and $6^2\Sigma^+$ have relatively smooth KER spectra starting above 2 eV. Again, the influence of high-lying $^2\Sigma$ states, not considered in the simulation, cannot be excluded.
The dissociation fractions are plotted in Fig. S13. For $3^2\Sigma^+$ and $D^2\Pi$, the dissociation process still continues after 1 ps due to tunneling and nonadiabatic transitions, respectively. For other states, the dissociation process is finished within 1 ps and the difference between the final dissociation fraction and unity is equal to the fraction which dissociates to the $C + O^+$ limit.

3.6 Dissociation-ratio corrected photoionization yields

In order to compute the photoionization yields observed in the experiment, the raw photoionization yields need to be multiplied by the respective dissociation ratios. For $9^2\Pi$ the nuclear dynamics is not available. Since the state lies among many high-energy dissociative states, which are typically strongly coupled, the ionization ratio of 0.5 is assumed, attributing 50% dissociation to $C^+ + O$ and 50% to $C + O^+$. Due to similarity of the raw photoionization yields to the C and O sides, the yields shown in Fig. S15 are averaged over the C and O signal. For the parallel orientation, the $3^2\Sigma^+$ state still has the highest yield but closely followed by the $4^2\Sigma^+$ and other states. In the perpendicular orientation, the $5^2\Sigma^+$ state has slightly higher yield than the $3^2\Sigma^+$. In addition, the relative yield of $^2\Pi$ states is higher in the perpendicular orientation than in parallel orientation.
To calculate the relative contributions of each state to specific sideband signals, the dissociation-ratio corrected yields have to be multiplied by the appropriate XUV peak intensities. Interestingly, according to MR-CIS I_p shown in Table S4, the energy spacing between states is such that all the states can contribute to a single band, since the highest difference of energies of all states contributing to the same sideband is only 1.45 eV. This leaves enough space to form well separated sidebands and mainbands in the RABBITT spectrum. The resulting relative contributions of the considered states to the RABBITT

sidebands are shown in Fig. S16. Because of their higher I_p, the high lying states ($4^2\Sigma^+$, $5^2\Sigma^+$, $6^2\Sigma^+$ and $9^2\Pi$) contribute significantly only to low-energy sidebands, despite their relatively large cross sections at higher energies.Thus, in the parallel orientation, the spectrum is dominated by the $4^2\Sigma^+$ state at low energies and by the $3^2\Sigma^+$ state at high energies. In the perpendicular orientation, on the other hand, the contribution of states is more balanced with $5^2\Sigma^+$, $3^2\Pi$ and $3^2\Sigma^+$ dominating the signal at some energy.

3.7 Orientation-dependent stereo Wigner time delays

Following the experimental analysis, the perpendicular spectrum can be split according to the KER into two groups: 1) low KER corresponding exclusively to $3^2\Sigma^+$ and $D^2\Pi$ in the theoretical treatment, and 2) high KER corresponding to all other states. The relative contributions of states to KER-resolved perpendicular spectra are shown in Fig. S14. In the low-KER spectrum roughly the $3/4$ of the signal are due to $3^2\Sigma^+$ and 1/4 due to $D^2\Pi$. More states contribute to the high-KER spectrum at low energies, while at high energies the signal comes almost exclusively from $3^2\Pi$.

Knowing the relative contributions of each state to a specific sideband, the sideband central position and the related stereo-photoionization time delays can be calculated approximately as weighted averages of state-specific sideband position and stereo-photoionization delays, respectively. The sidebands energy position corresponds to the data points shown in Fig. S17. At low energies the delays in the perpendicular orientation agree with high-KER experimental delays. This supports the fact that at low energies high-I_p states dominate the sideband signal. At high energies, on the contrary, the perpendicular delays agree with the low-KER delays, since electrons from high-I_p states do not appear at high energies, considering the experimental XUV spectrum.

Fig. S18 shows position-space cuts of the DO corresponding to different ionic states. Apart from the clear bias of the DO of $9^2\Pi$ state towards the oxygen atom, it is difficult to see a clear pattern for the other states . Fig. S19 shows two-dimensional phase-space projections of Wigner functions of the dipole transition matrix (DTM) of the DO with the polarization parallel to the molecular axis. For $^2\Sigma$ states both position q and momentum p are also parallel to the molecular axis. For $^2\Pi$ states, both q and p are inclined from the molecular axis by 30 degrees. In the case of $^2\Sigma$ states, the bias towards carbon is clearly visible. The asymmetry of all three $^2\Pi$ states is reversed towards oxygen even though it is not pronounced for $D^2\Pi$ and $3^2\Pi$. Fig. S19 shows the Wigner functions of the DTM with the polarization in the direction perpendicular to the molecular axis. Positions q and momenta p are inclined from the polarization axis by 30 degrees, for both $^2\Sigma$ and $^2\Pi$.

3.8 Mean position of ionization

There are two main possible sources of the asymmetry of the photoionization time delays: the asymmetry of the electrostatic potential of CO^+ and the asymmetry of the wave function of the ionizing electron. The first source does not seem to be decisive since no clear correlation can be found between the state-specific stereo-photoionization delays (see Fig. S10) and the dipole moments of ionic states listed in Table S7.

The simplest measures of the asymmetry of the wave function of the ionizing electron along the molecular axis are the mean position of the DO and the DTM summarized in Table S7. While the mean position of the DO can be thought of as the average equilibrium position of the electron before ionization, the mean position of the DTM can

be though of as the average position from which the electron actually ionizes. Table S7 reveals that whereas there is a very weak correlation between the asymmetry of the DO and the stereo photoionization time delay, the correlation between the asymmetry of the DTM and stereo delay is quite strong in the parallel orientation. In accordance with the observations already made on plots of Wigner functions of DTMs (Fig. S19), all four $^2\Sigma$ states ionize mostly from the carbon side. On the contrary the $D^2\Pi$ and $3^2\Pi$ states ionize relatively close to the center of the molecule with a bias towards the oxygen atom. The $9^2\Pi$ state ionizes from the vicinity of the oxygen atom. The correlation between the DTM and stereo delay in the perpendicular orientation is weaker than in the parallel case.
Even though the mean position $\langle q \rangle$ of the DTM correlates quite well with trends observed in stereo delays, the disadvantage of this quantity is that it averages over electrons ionizing with all possible energies and also over electrons which merely get excited to another bound state. To overcome this limitation, energy-resolved mean positions of ionization $\langle q_I(E) \rangle$ were computed with the classical Wigner method. Fig. S20 shows that for most states the highest $\langle q_I(E) \rangle$ absolute values appear at low energies. At low energies, $4^2\Sigma^+$, $5^2\Sigma^+$and $9^2\Pi$ ionize from the outer positions well beyond the carbon and oxygen atoms, respectively. As will be demonstrated later, the fact that – at low energy in the parallel orientation – the electron ionizes further away from the center of the molecule, agrees very well with computed stereo delays and observed strongly negative stereo delays. Another distinct feature revealed in the energy resolved $\langle q_I(E) \rangle$, is that all $^2\Sigma$ states except for $4^2\Sigma^+$ cross from negative to positive values of $\langle q_I(E) \rangle$ at higher energies and that $\langle q_I(E) \rangle$ (for all states except for $D^2\Pi$) moves towards the oxygen nucleus (located at 1.07 au) with increasing energy. Both facts suggest that oxygen becomes increasingly important as the source of higher-energy electrons. Again this fact correlates well with the observed shift from negative to positive delays at higher energies in the parallel orientation.
To better judge correlations between $\langle q_I(E) \rangle$ and stereo delays, the mean position of ionization $\langle q_I(E) \rangle$ is converted to the simple mean stereo-delay $\tau_{\langle SW \rangle}$ as follows:

$$\tau_{\langle SW \rangle}(E) = \frac{2\langle q_I(E) \rangle}{\sqrt{(2E)}} \quad \text{(S11)}$$

where E is the final kinetic energy of the ionized electron. The factor of two in Eq. (S11) reflects the fact that in order to get to the equivalent position on the other side of the molecule, the electron has to cross the distance equal to $2q_I$. The comparison of $\tau_{\langle SW \rangle}(E)$ with stereo-photoionization delays is shown in Fig. S21. When CO is oriented parallel to the polarization of the field, both quantities correlate surprisingly well (especially for higher absolute delays), pointing to a straightforward connection between observed stereo-photoionization delays and mean positions of ionization. Interestingly, very good match is obtained when the final velocity of the ionized electron $\sqrt{(2E)}$ is used directly used, neglecting the details of the CO^+ potential. The correlation between stereo photoionization time delays and ionization positions is weaker in the perpendicular case since: a) for smaller delays, details of the potential energy surface become relatively more important; b) the asymmetry of the potential acts in the transverse direction to the propagation of the ionizing electron, bending the trajectory and obfuscating the information about the initial direction after ionization.

3.9 General applicability of the Stereo Wigner time delay

In order to asses the generality of our observations, we computed the stereo-delays for the ionization of nitric oxide from the ground state into the two lowest $^3\Pi$ states. The Dyson orbitals were computed using CASSCF(9,10)/aug-cc-pVTZ for the neutral NO and CASSCF(8,10)/aug-cc-pVTZ for the NO^+ ion. The potential of NO^+ was approximated with the multipole expansion up to octupole level. The results are shown in Fig. S23. The two considered states ionize preferentially from the opposite side of the molecule and for both the simple mean stereo-delay $\tau_{\langle SW \rangle}(E)$ agrees very well with the stereo-delay τ_{SW}. Therefore, similar as in the case of CO, the position of ionization seems to be the most important determining factor for the photoionization delay in NO.

3.10 Analysis of the axial recoil approximation

The experimental data-analysis relies on the assumption that the axial recoil approximation is sufficiently valid to retrieve the angular information upon photoionization. This approximation is valid when the dissociation is sufficiently fast compared to molecular rotation, so that the recoil angle of the fragment coincides with the bond along which the molecule dissociates (*28*). Primary causes for obscuring the angular information is the rotational temperature of the beam and the dissociative lifetime.

The estimated temperature of the CO cold jet was estimated to be $T \sim 5 - 10$ K. We can determine the most probable occupied rotational level from the Boltzmann distribution under this condition as:

$$L_{\max} = \sqrt{\frac{kT}{2B}} - \frac{1}{2} = \sqrt{TI} - \frac{1}{2}, \quad \text{(S12)}$$

where k is the Boltzmann constant equal to unity in the atomic units, B is the rotational constant, I is the moment of inertia $I = \mu r^2$, μ is the reduced mass of the molecule ($\mu = 12505.97$ au for CO) and r the bond length. Considering $T = 10$ K and an equilibrium bond length of the CO molecule $r_0 = 2.1316$ au, the most probable angular momentum is $L_{\max} = 0.84$. Substituting $L_{\max}$ into the definition of the angular momentum as follows

$$L_{\max} = r \times p = I\omega_0 \quad \text{(S13)}$$

we obtain the classical most probable angular frequency $\omega_0 = 1.48 \cdot 10^{-5}$ a.u. and the corresponding rotational period $T_0 = 10.3$ ps. These values serve as a rough estimation, given the quantum character of the molecular rotation at such a low temperature. During dissociation, in the absence of torque (neglecting the effects of the weak IR probe field), the angular momentum L is conserved. Therefore, the actual angular frequency ω may be computed as:

$$\omega = \frac{L}{\mu r^2} = \frac{c_\omega}{r^2}, \quad \text{(S14)}$$

where c_ω can be determined using the equilibrium values ω_0 and r_0. The total angle of rotation θ of the molecular axis from the instant of ionization t_0, may be computed as:

$$\theta = \int_{t_0}^{\infty} \omega \, dt = c_\omega \int_{t_0}^{\infty} \frac{1}{r(t)^2} \, dt. \quad \text{(S15)}$$

Looking at Figs. S8 and S9 one realizes that the PESs of dissociative states are almost constant for $r > r_c = 10$ au $= 5.29$ Å. (Note that r_c is chosen arbitrarily in the region where PES can be considered approximately constant, choosing a higher value of r_c would lead to an overestimation of θ.)
Since the acceleration of the wave packet occurs between r_0 and r_c, it is thus reasonable to split Eq. (S15) into two parts

$$\theta = \theta_c + \theta_\infty = c_\omega \left(\int_{t_0}^{t_c} \frac{1}{r(t)^2} dt + \int_{t_c}^{\infty} \frac{1}{r(t)^2} dt \right) \quad \text{(S16)}$$

The radial velocity acquired during dissociation, v_c, can be is estimated using the final KER spectra (Fig. S12) as $v_c = \sqrt{2E_c}$. It shows that the velocity of the nuclei due to molecular rotation is at least two orders of magnitude smaller than v_c. Therefore, it can be neglected in the treatment of the radial motion.
Beyond r_c the radial motion corresponds to a free particle $r(t) = r_c + v_c(t - t_c)$, where t_c is the time at which the wave packet reaches r_c. An upper limit for θ was obtained, using the kinetic energy E_c of the low KER peak (summarized in Table S7) of each KER spectrum (see Fig. S12).
In order to determine the angle of rotation θ_c, the motion $r(t) = r_0 + a(t - t_0)^2/2$ with constant acceleration a is assumed, with the exception of $D^2\Pi$. The shape of the PESs (Figs. S8 and S9) reveals that the motion with constant acceleration overestimates θ_c for directly dissociating wave packets. The actual PESs, in fact, accelerate the wave packet mostly at the beginning of the dissociation where ω is the highest. In contrast to other states, a significant portion ($\sim 50\%$) of $D^2\Pi$ population oscillates prior to the dissociation process. Therefore, we simply assume $r(t) = r_0$ while computing θ_c for the $D^2\Pi$ state, which would overestimate θ_c. The time t_c it takes to reach r_c is estimated from Fig. S13, which shows the normalized wave packets past r_c during the 1-D quantum simulation of CO^+ dissociation.
The upper limit for θ is estimated considering t_c as the time when $\sim 90\%$ of the ionizing wave packet is beyond r_c (Table S8). Note that since Fig. S13 shows the dissociation ratio into the $C^+ + O$ channel, the final value of the dissociation ratio is in all cases < 1. Therefore, in order to determine t_c, 90% of the value attained at 1 ps is used. The $D^2\Pi$ state is not fully dissociated after 1 ps, therefore t_c was determined by an extrapolation of the dissociation ratio. For the $3^2\Sigma^+$ state, contributions dissociating after 1 ps were neglected as these originate from a slow tunneling process.
Once t_c is estimated, the acceleration a is determined according to $a = \sqrt{2\mu E_c}/t_c$ (similar results were obtained using other approaches to determine a). The integrals in Eq. (S16) can be evaluated as

$$\theta_\infty = \int_{t_c}^{\infty} \frac{c_\omega}{[r_c + v_c(t - t_c)]^2} dt = \frac{c_\omega}{v_c r_c} \quad \text{(S17)}$$

$$\theta_c = \int_{t_0}^{t_c} \frac{c_\omega}{[r_0 + a(t - t_0)^2/2]^2} dt = \frac{1}{\sqrt{2a} r_0^{3/2}} \arctan\left[\sqrt{\frac{a}{2r_0}} (t_c - t_0) \right] + \frac{t_c - t_0}{a r_0 (t_c - t_0)^2 + 2r_0^2}$$

$$\theta_c(D\,^2\Pi) = \int_{t_0}^{t_c} \frac{c_\omega}{r_0^2} dt = \frac{c_\omega}{r_0^2} (t_c - t_0)$$

giving the total angle of rotation of the molecular axis after ionization $\theta = \theta_c + \theta_\infty$ (summarized in Table S9). In all cases, θ_c is the most important contribution as $\theta_\infty \lesssim 0.3°$. For all higher-energy excited states not explicitly considered in this analysis, one may assume $\theta < 1°$, since high excited states typically i) dissociate quickly due to the excess energy and ii) the abundance of nonadiabatic transitions to lower lying states.
We now discuss the actual impact of the molecular rotation when applying the axial recoil approximation to define the molecular axis. In both cases, parallel and perpendicular, the acceptance angle with respect to the field polarization is $20°$ and the detection angle of the ionized electrons is $60°$ from the field axis.
In parallel orientation, the only effect of a rotation less than $70°$ is the "smearing out" of the molecular axis acceptance cone. Such a broadening is due to the fact that some molecules oriented within the $20°$ cone at the moment of ionization appear outside of the cone due to molecular rotation and vice versa. Clearly all angles summarized in Table S9 (with an exception of $D^2\Pi$) are too small to have a significant measurable effect. We have computed that opening the detection cone from $10°$ to $20°$ changes the stereo time delay by ~ 1 as for sideband 16 of $3\,^2\Sigma^+$ state in parallel orientation.
In the case of perpendicular orientation, the effect of rotation is twofold: 1) there is a "smearing out" of the detection cone (similar to the parallel orientation) and 2) the incorrect assignment of the ionization side (C or O) for electrons which ionize very close to $90°$ from the molecular axis (again with an exception of $D^2\Pi$). However, these electrons do not contribute to the measured stereo Wigner time delay, as the contribution of electrons at $90°$ is zero.
In this analysis, one state requires special attention. The state with the highest θ is $D^2\Pi$. Roughly 50% of the state ionizes directly, which yields θ to be very small. Instead for the remaining 50% the axial recoil approximation breaks down. Fortunately, two factors alleviate this problem: 1) the stereo Wigner time delays of $D^2\Pi$ are close to zero, 2) the inhomogeneity of the angular distribution of $D^2\Pi$ stereo Wigner time delays is smaller than the experimental resolution. The main effect of the slowly dissociating $D^2\Pi$ state is the lowering of the observed stereo Wigner time delays of the $D\,^2\Pi$ state in the perpendicular orientation.

Fig. S1.

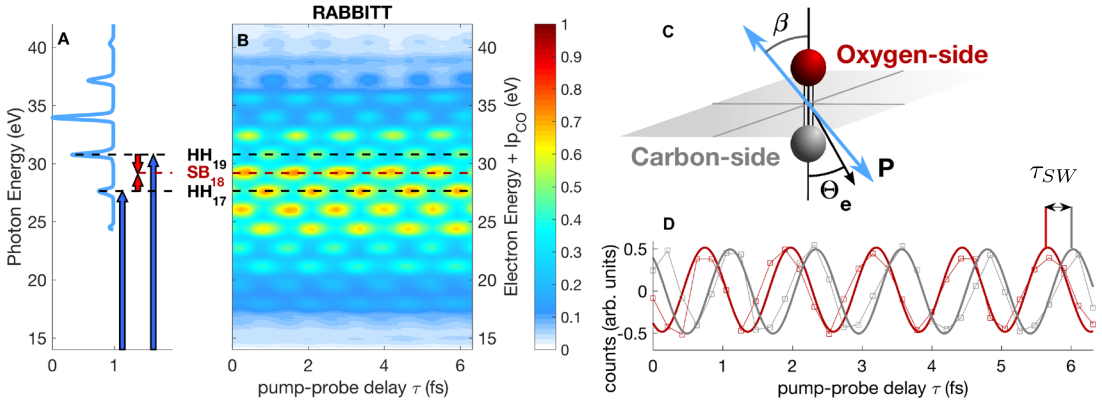

Fig. S1. RABBITT principle explained for the CO molecule. (**A**) Single photon transitions (blue arrows) induced by the extreme-ultraviolet (XUV) pulse (blue curve) appear as high-order harmonics (HH), whereas superimposing the infrared (IR) field (red arrows) results in two-photon transitions, forming sidebands (SBs) in the photoelectron spectrum. (**B**) The spectrogram shows the integrated photoelectron spectrum recorded as a function of the pump-probe delay $\boldsymbol{\tau}$. The black and red dashed lines indicate HH and sidebands, respectively. (**C**) The orientation of the molecular axis with respect to the laboratory frame, defined by the polarization axis **P** (blue arrow) is given by the angle $\boldsymbol{\beta}$. The emission angle of the photoelectron (black arrow) within the molecular frame is defined as $\boldsymbol{\Theta_e}$. (**D**) Photoelectron spectra are separated according to the escaping side of the photoelectron within the recoil frame. Sidebands are projected onto the delay axis (squares) and frequency filtered by a fast-Fourier transform (solid, thick line). After fitting the sideband-signal, the molecular specific scattering phase $\boldsymbol{\Delta\varphi_{tot}}$ of the photoelectron escaping on the oxygen-side of the molecule (gray curve) is compared with the photoelectron escaping on the carbon-side (red curve). The difference in scattering phase is used to access the stereo Wigner time delay $\boldsymbol{\tau_{SW}}$.

Fig. S2.

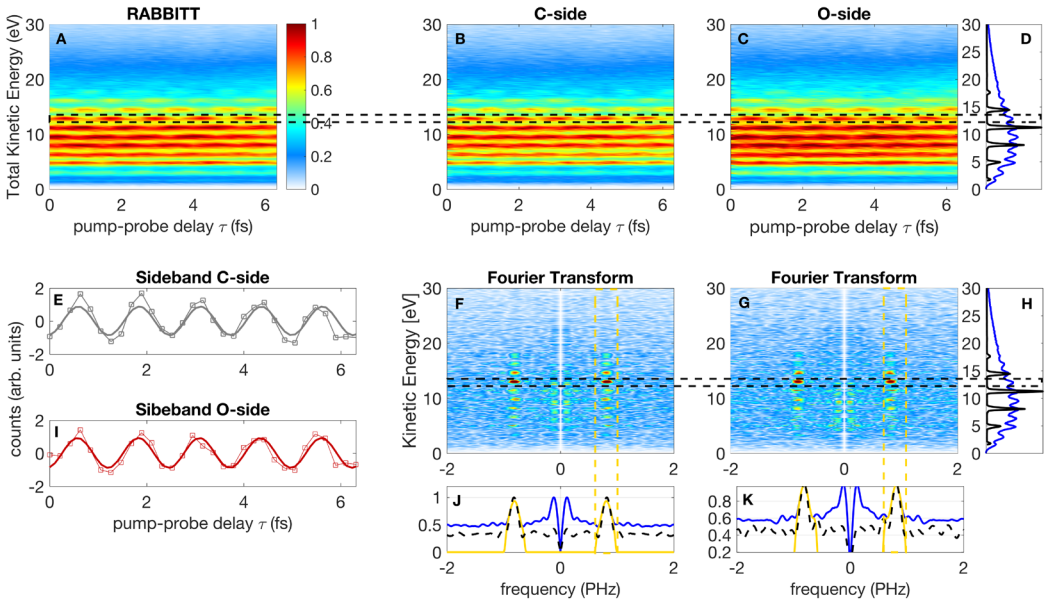

Fig. S2. Extraction of stereo Wigner time delay. (**A**) shows the photoelectron RABBITT trace selected on the coincident ion time of flight corresponding to the C^+-fragment. The photoelectron spectrum is shown as a function of pump-probe delay $\boldsymbol{\tau}$. Further selecting the emission angle of the photoelectron with respect to the polarization axis $\boldsymbol{\theta_e}$, allows us to separate photoelectrons escaping on carbon-side (**B**) and oxygen-side (**C**). Contributions stemming from the high harmonics are matched with the XUV spectrum (**D, H**) using the rules $\boldsymbol{h\nu = E_e + Ip}$ and $\boldsymbol{h\nu = KER + E_e + DL}$, where $\boldsymbol{h\nu}$ is the photon energy, $\boldsymbol{E_e}$ the electron kinetic energy, $\boldsymbol{KER}$ the kinetic energy release, $\boldsymbol{Ip}$ is the ionization potential and $\boldsymbol{DL}$ the dissociation limit of the corresponding state. In such a way we can verify the contributions belonging to the so-called sidebands. We select each sideband to be integrated over a specific energy range indicated by the black-dashed lines. The Fourier transformed signal and its projection is windowed (yellow-dashed lines) before converted back to the time-domain, as shown in (**F, J**) and (**G, K**). The raw (square-dashed) and Fourier-filtered (solid) sideband signals for each sideband are displayed (**E, I**), separated according to $\boldsymbol{\theta_e}$ (oxygen-side in red, carbon-side in grey).

Fig. S3.

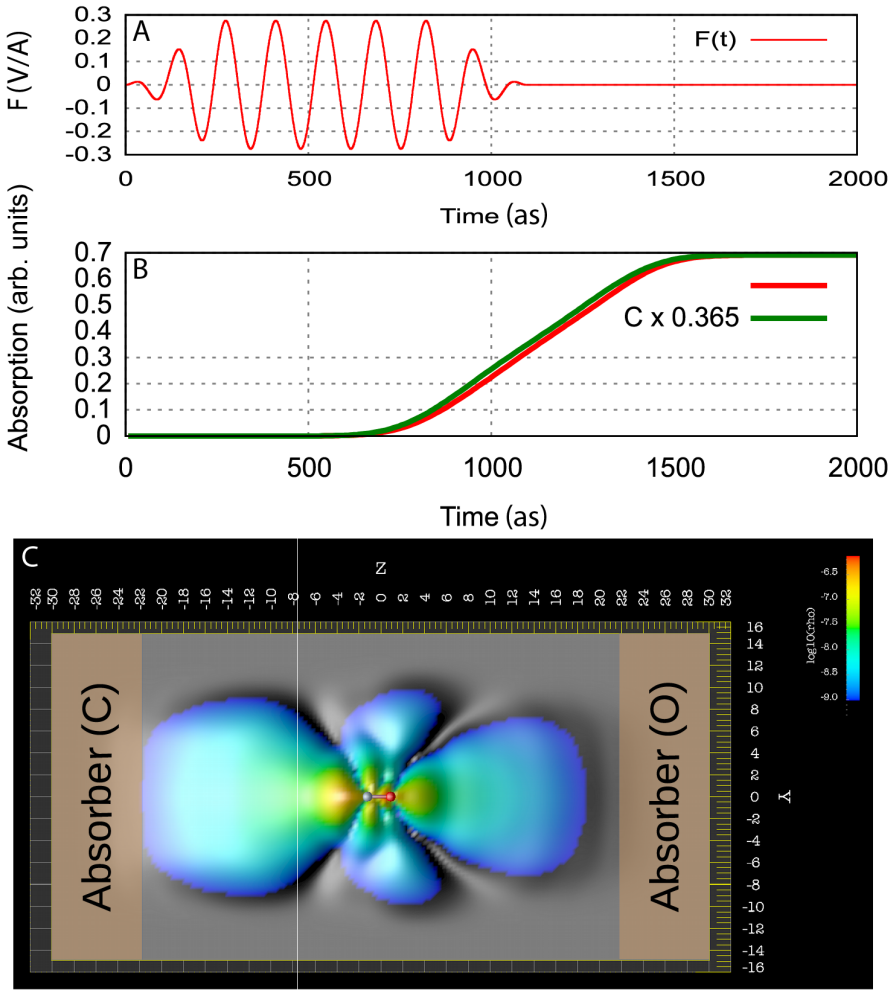

Fig. S3. Electron time-of-flight simulation for the ground-state ionization channel of CO. (A) Electric field profile for the 9-cycle flat-top XUV pulse (H19, Table S2). The pulse is polarized along the Z direction. (B) Probability of an electron reaching the absorber as a function of time, in arbitrary units. Green (upper) curve: probability of reaching the absorber at negative Z (carbon end). Red (lower) curve: probability of reaching the absorber at positive Z (oxygen end). The carbon curve has been scaled by a factor 0.365. (C) Probability density of the active electron at the time t=650 as. The contribution due the channel Dyson orbital has been subtracted. The probability density (in $Bohr^{-3}$) is measured in the YZ plane, 0.18 Bohr below the plane containing the nuclei. The wavefunction on the negative-Z (carbon) end of the molecule is already being absorbed. The wavefunction on the positive-Z (oxygen) end still have not reached the absorber. The Y and Z coordinate axes are given in Bohr.

Fig. S4.

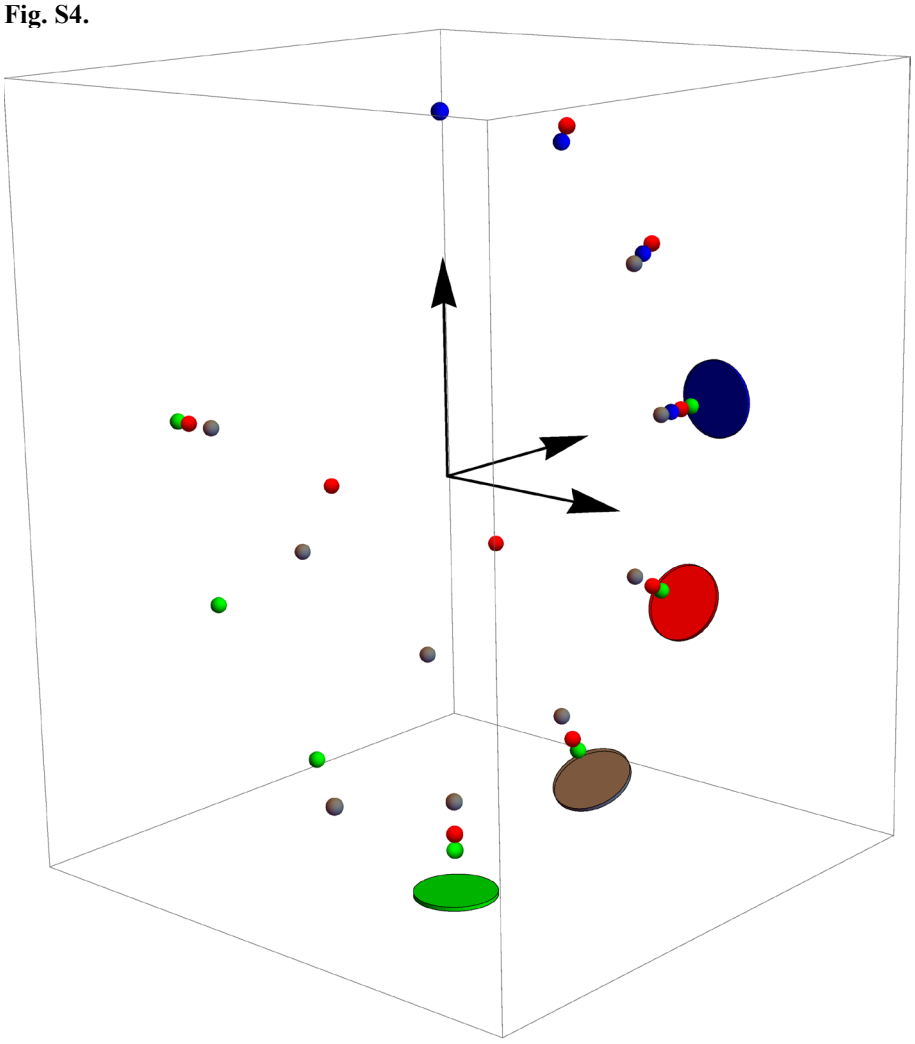

Fig. S4. Computational geometries represented in the laboratory frame of reference. The laser electric field is along the Z axis, pointing towards the blue disk. The disks represent the absorber in the positive local-Z direction. The corresponding negative local-Z absorber is at the position symmetric with respect to the origin (not shown). Each directional absorber is associated with several possible orientations of the molecular axis, given as a sphere of the same colour.

Fig. S5a.

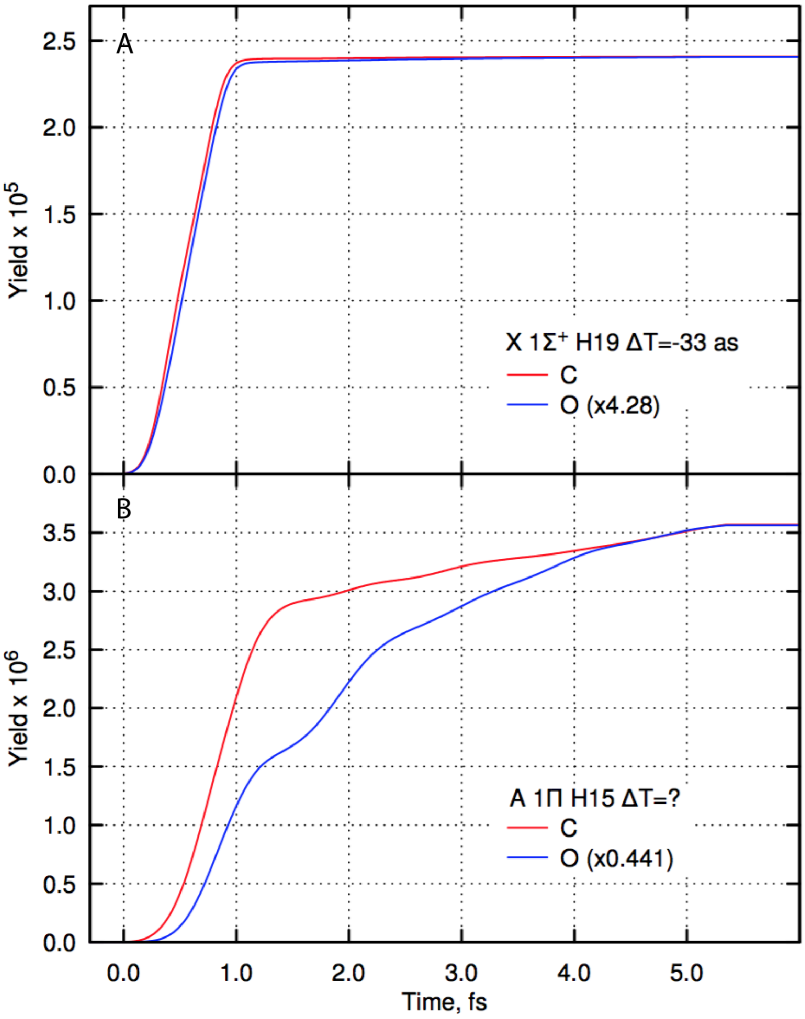

Fig. S5a Time profile of electron probability reaching the detector. The yields are given in electrons per CO molecule. The differential arrival times have been corrected for the dipole effects Eq (S2). (**A**) Electrons correlated to the **X** $\mathbf{1^2\Sigma^+}$ ion state, harmonic 19. Time profiles have identical shape for the detector on the oxygen and carbon sides. (**B**) Electrons correlated to the **A** $\mathbf{1^2\Pi}$ ion state, harmonic 15. Time profiles have complex, distrinct shares for each detector. Time delay can not be extracted.

Fig. S5b.

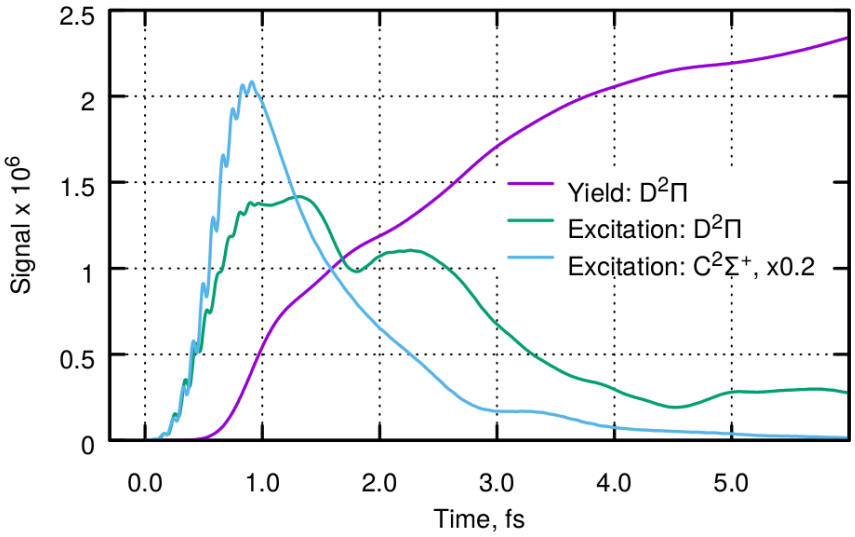

Fig. S5b Origin of the complex time dependence in ionization signal. The total ionization yield in the **D $2^2\Pi$** channel (purple line), integrated over all photoelectron directions, is shown for the laser field polarized perpendicular to the molecular axis for the H15 XUV field. The total population of the excited and continuum states within the simulation volume is shown with the green (**D $2^2\Pi$** channel) and teal (**C $3^2\Sigma^+$** channel, scaled by 0.2). At the central photon energy of the H15, the **C $3^2\Sigma^+$** ionization channel is closed, causing autoionizing Rydberg states to be populated at the **C $3^2\Sigma^+$** threshold. Decay of these states dominates continuum population in the **D $2^2\Pi$** channel after the end of the XUV pulse (time > 1 fs), leading to the complex photoelectron signal in the **D $2^2\Pi$** channel**,** and causing large apparent photoelectron delays. Please note that our simulation underestimates the natural lifetimes of high Rydberg states due to the finite extent of the simulation volume (see text).

Fig. S6a.

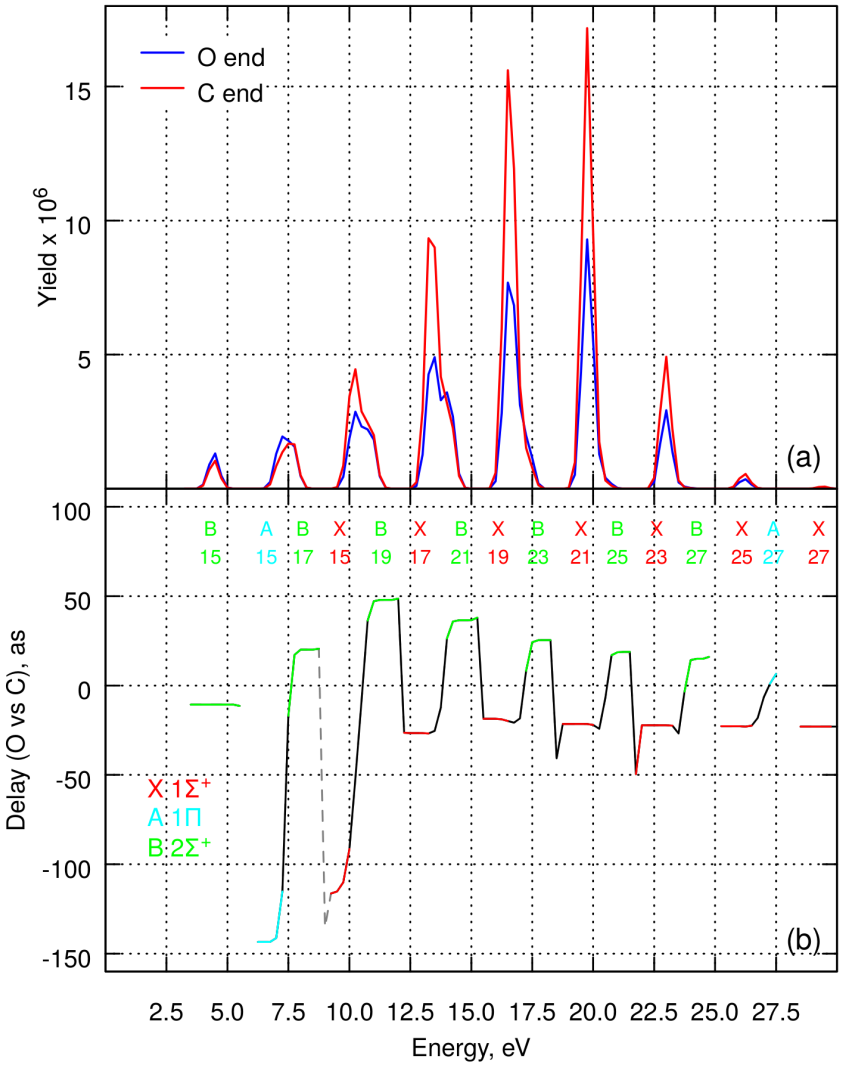

Fig. S6a Simulated photoelectron and directional time delay spectra correlated to stable CO^+ molecular ions. The simulation includes **X $1\Sigma^+$**, **A 1Π**, and **B $2\Sigma^+$** states (Table S3), pulse P1 (Table S2), and parallel orientation of the molecular axis relative to the laser polarization direction. The photoelectron spectrum is accumulated incoherently with respect to the final ion state. (**A**) Photoelectron signal on the oxygen-side (blue line, eq. (S3)) and carbon-side (red line, eq. (S4)) detectors. (**B**) Apparent delay of the oxygen-side signal (attoseconds). Dashed segments of the line indicate photoelectron energies where the simulated delay is unreliable due to the complex time dependence of the signal. Colored segments indicate parts of the delay spectra where the dominant ionization channel contributes at least 70% of the overall photoelectron signal.

Fig. S6b.

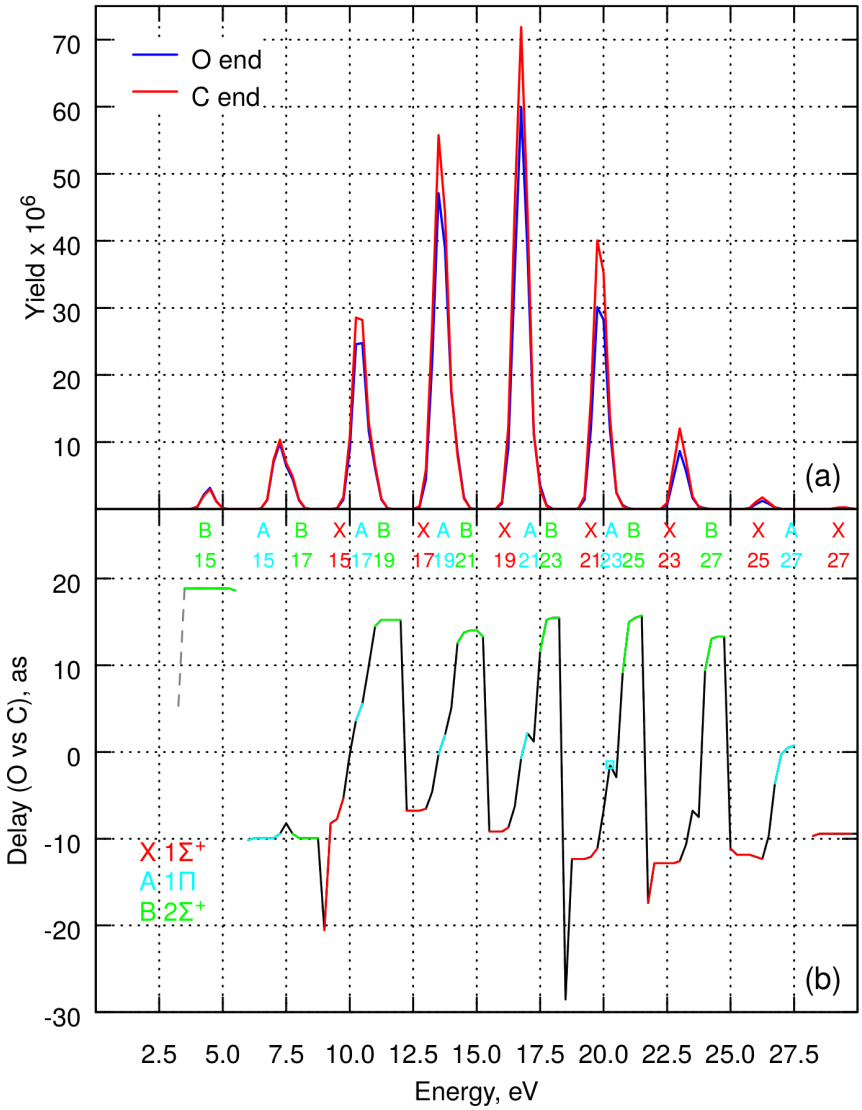

Fig. S6b Simulated photoelectron and directional time delay spectra correlated to stable CO^+ molecular ions. As is Fig S6a, but for the molecular axis perpendicular to the laser polarization direction (Eqs. (S5)-(S6)).

Fig. S7a.

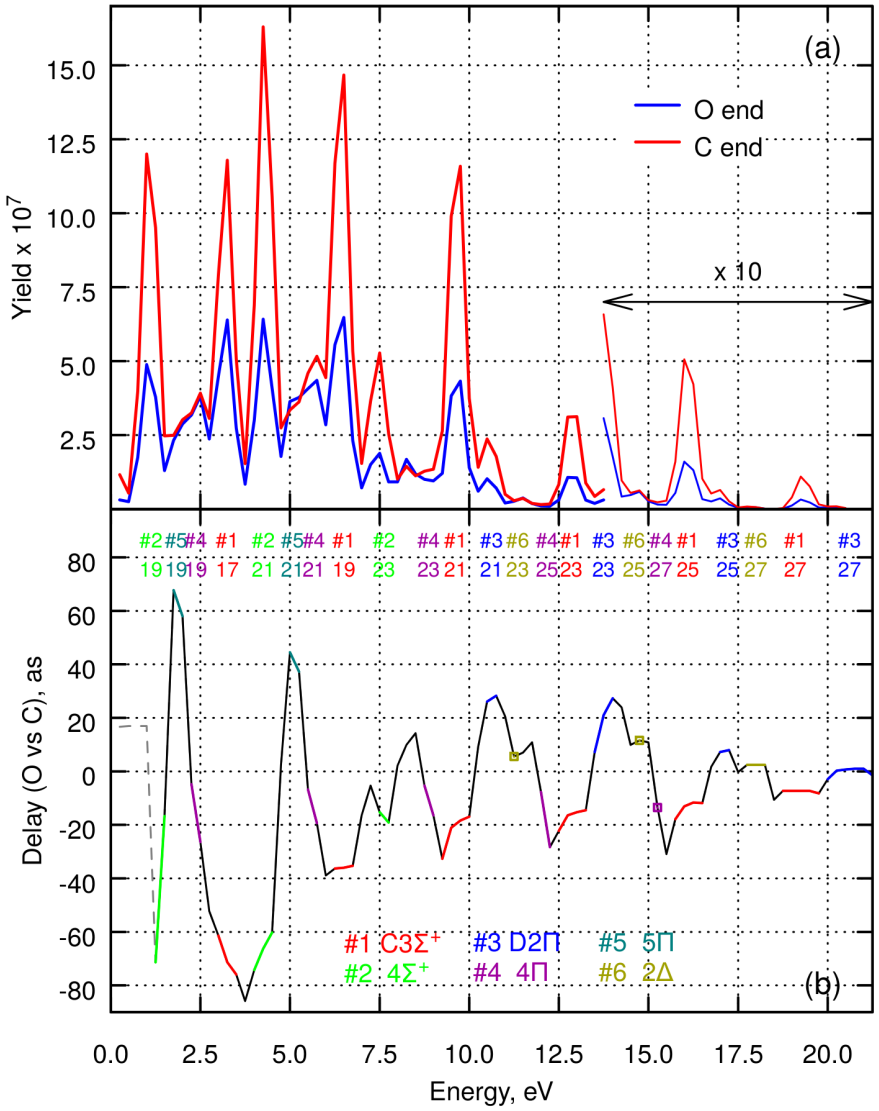

Fig. S7a Simulated photoelectron and directional time-delay spectra correlated to the $C^+ + O$ fragmentation channel. The simulation includes **C $3^2\Sigma^+$**, **D $2^2\Pi$**, **$1^2\Delta$**, **$2^2\Delta$**, **$3^2\Pi$**, **$4^2\Pi$**, and **$5^2\Pi$** states of the initially-prepared CO^+ molecular cation (Table S3) and pulse P1 (Table S2). Molecules are oriented along the laser polarization direction (Eqs. (S3)-(S4)). The photoelectron spectrum is accumulated incoherently with respect to the final ion state. See Fig. S6a caption for the panel descriptions.

Fig. S7b.

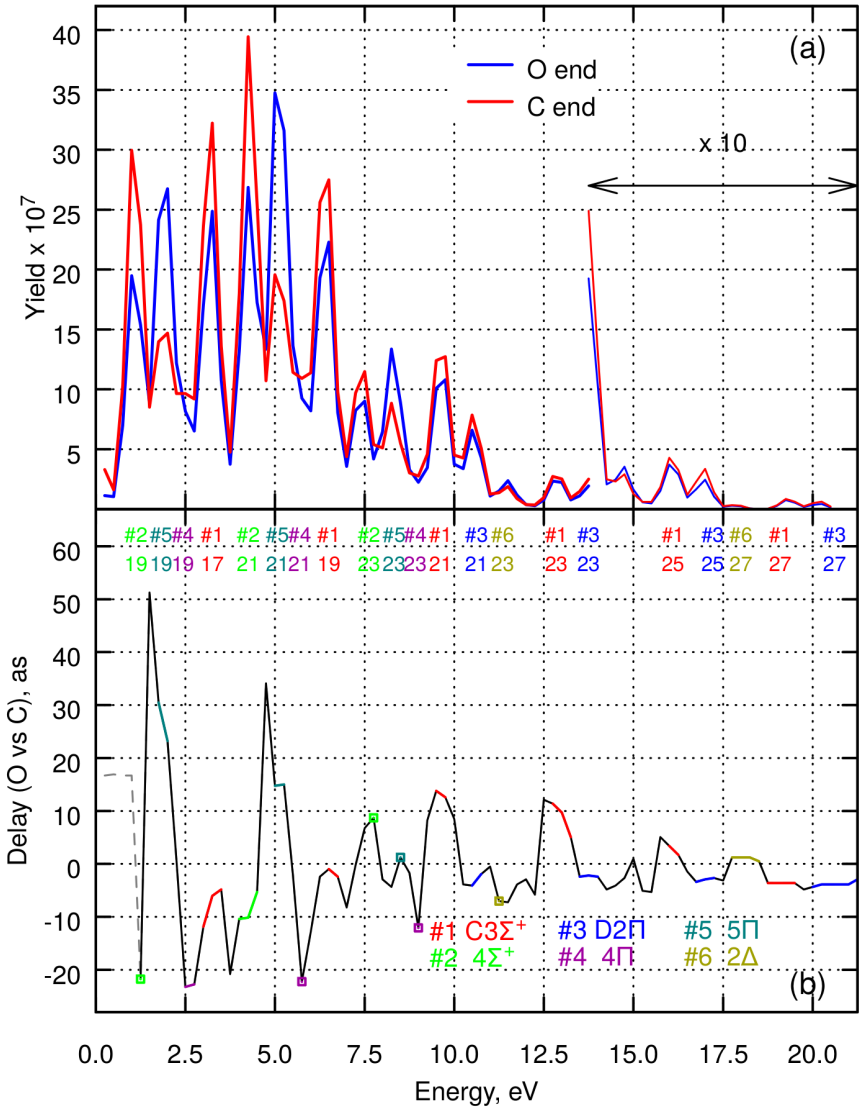

Fig. S7b Simulated photoelectron and directional time-delay spectra correlated to the $C^+ + O$ fragmentation channel. Molecules are oriented along the laser polarization direction (Eqs. (S5)-(S6)). See Fig. S6a caption for the panel descriptions.

Fig. S8.

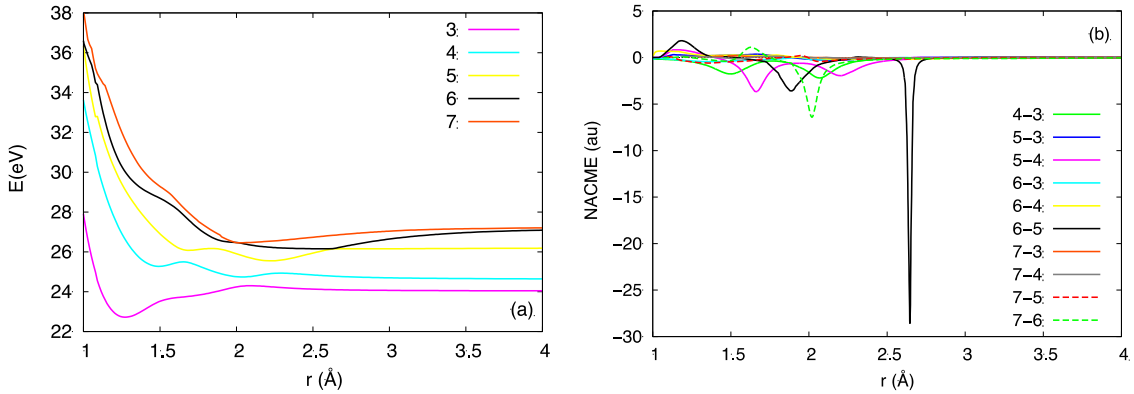

Fig. S8. Potential energy surfaces (PES) (**A**) and nonadiabatic coupling matrix elements (NACME) (**B**) used in the simulation of the dissociation dynamics of $^2\mathbf{\Sigma}$ states. The PES 3 refers to $\mathbf{3^2\Sigma^+}$, 4 to $\mathbf{4^2\Sigma^+}$, etc.

Fig. S9.

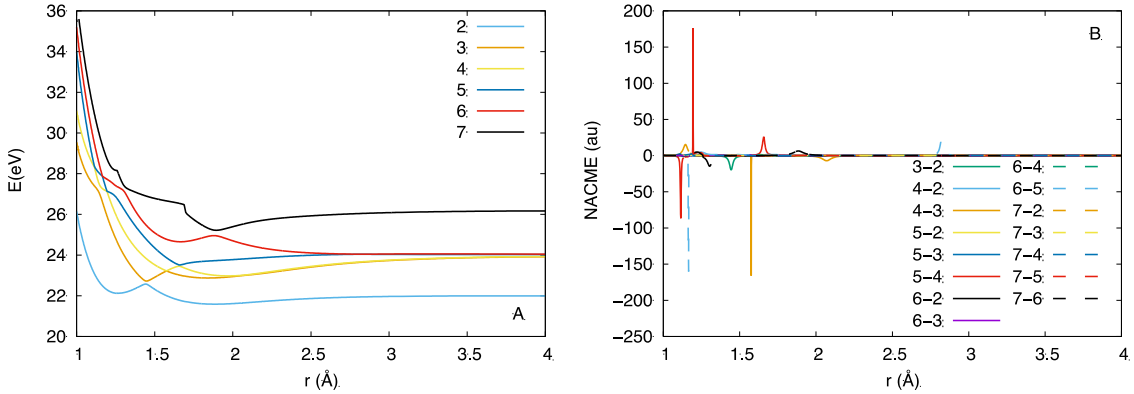

Fig. S9. Potential energy surfaces (PES) (**A**) and nonadiabatic coupling matrix elements (NACME) (**B**) used in the simulation of the dissociation dynamics of $^2\mathbf{\Pi}$ states. The PES 2 refers to **D** $\mathbf{2^2\Pi}$, 3 to $\mathbf{3^2\Pi}$, 4 to $\mathbf{4^2\Pi}$, etc.

Fig. S10.

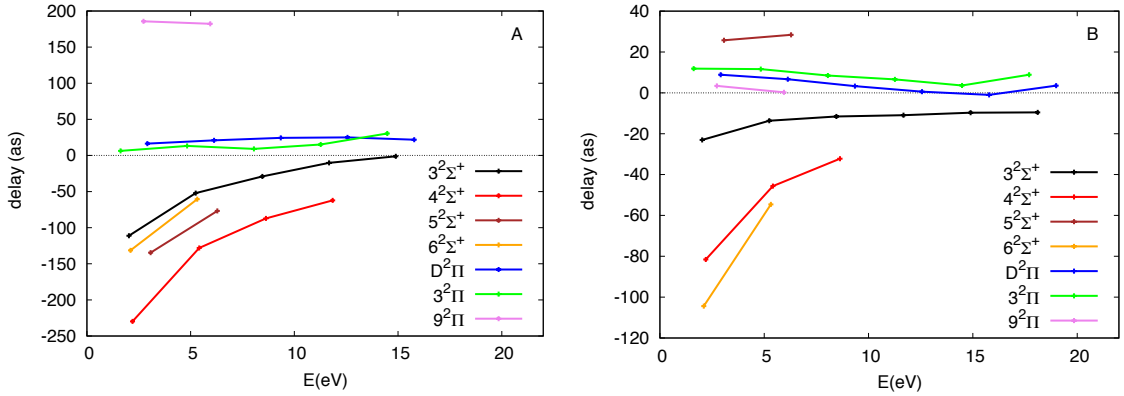

Fig. S10. Simulated stereo-photoionization delays of CO ionization channels. (**A**) CO axis is parallel to the polarization. (**B**) CO axis is perpendicular to the polarization. Statistical errors of the data points are equal to several as.

Fig. S11.

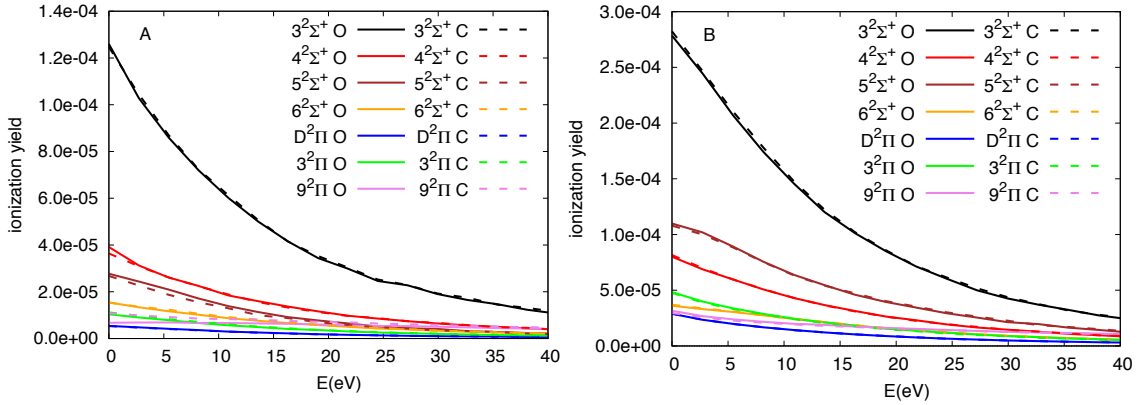

Fig. S11. Photoionization yields for electrons ionizing to the oxygen (O) and carbon (C) sides of CO. (**A**) CO axis is parallel to the polarization. (**B**) CO axis is perpendicular to the polarization.

Fig. S12.

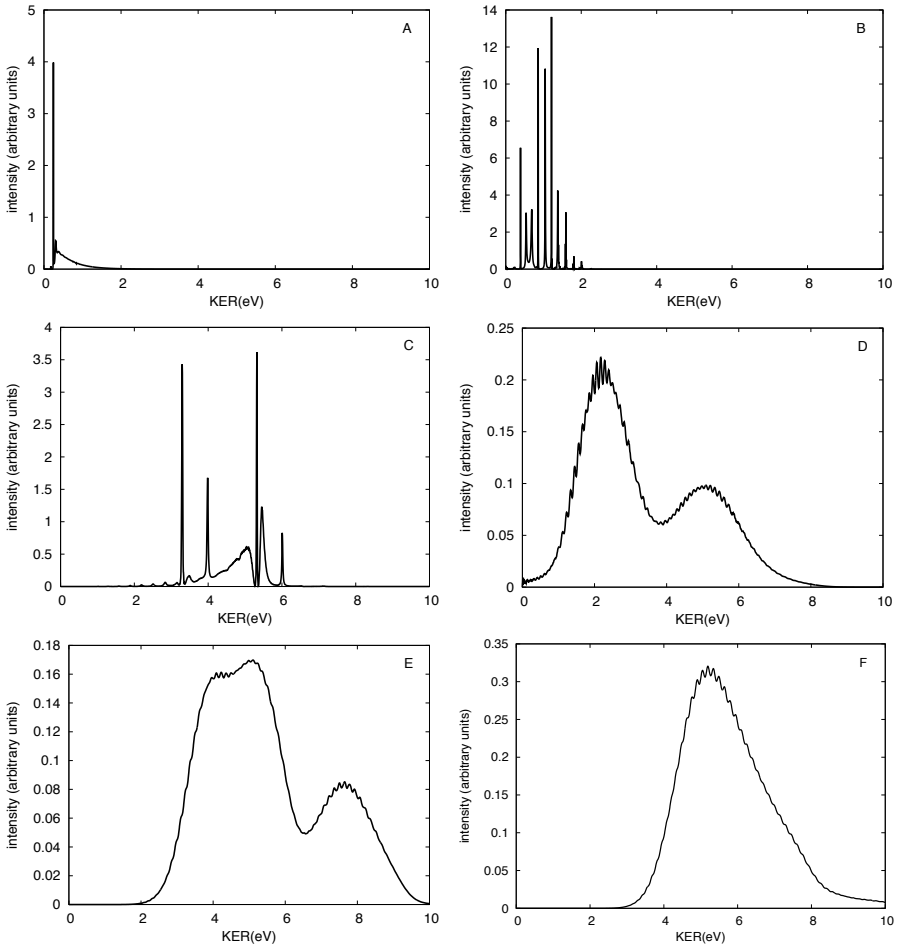

Fig. S12. KER spectra of $3^2\Sigma^+$ (A), $D^2\Pi$ (B), $3^2\Pi$ (C), $4^2\Sigma^+$(D), $5^2\Sigma^+$(E) and $6^2\Sigma^+$(F) states.

Fig. S13.

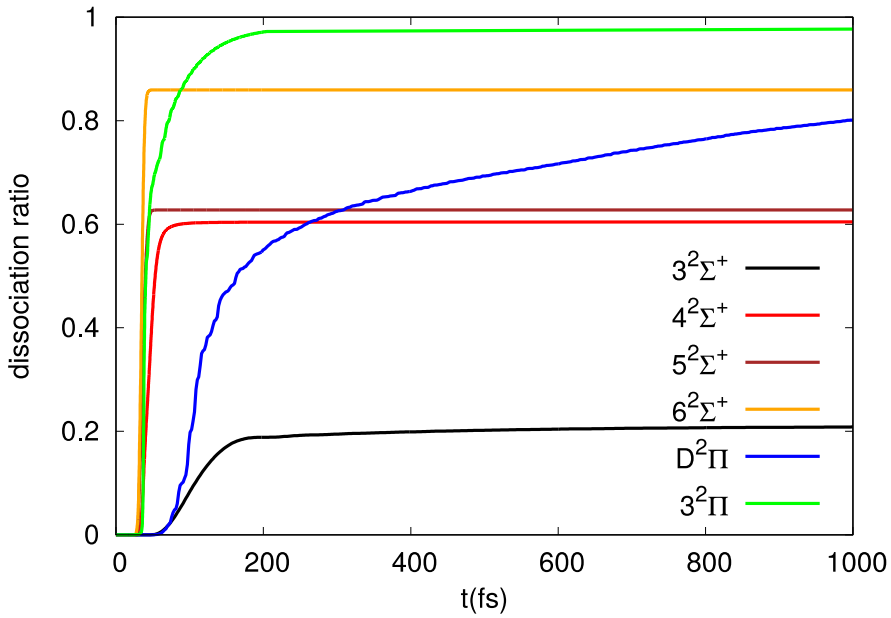

Fig. S13. Dissociation ratios of CO^+ states during the first 1 ps of the dissociation dynamics.

Fig. S14.

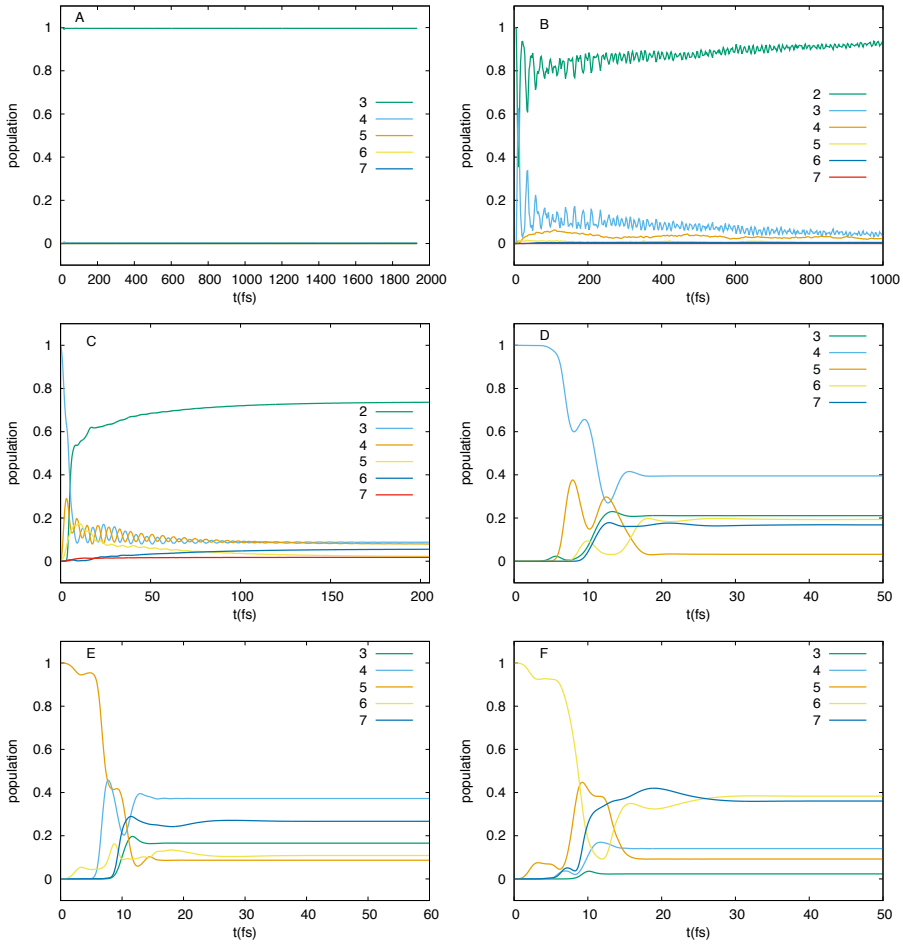

Fig. S14. Electronic state populations during the nonadiabatic propagation: $3^2\Sigma^+$ (A), $D^2\Pi$ (B), $3^2\Pi$ (C), $4^2\Sigma^+$(D), $5^2\Sigma^+$(E) and $6^2\Sigma^+$(F). For $^2\Sigma$ states, the population on PES 3 refers to $3^2\Sigma^+$, 4 to $4^2\Sigma^+$, etc. For to $^2\Pi$ states, the population on PES 2 refers to **D** $2^2\Pi$, 3 to $3^2\Pi$, 4 to $4^2\Pi$, etc.

Fig. S15.

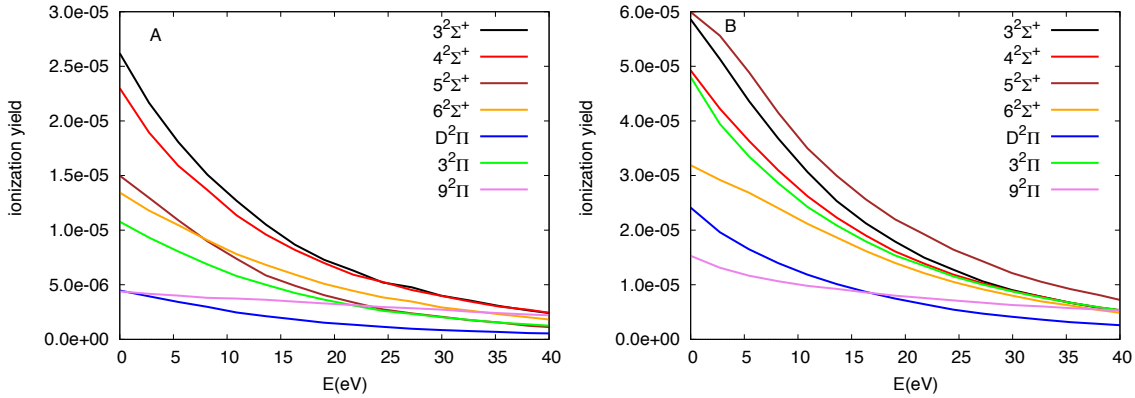

Fig. S15. Simulated ionization yields of CO orbitals taking into account CO dissociation ratios. (**A**) CO axis is parallel to the polarization. (**B**) CO axis is perpendicular to the polarization. Note that $\mathbf{9^2\Pi}$ dissociation ratio is estimated.

Fig. S16.

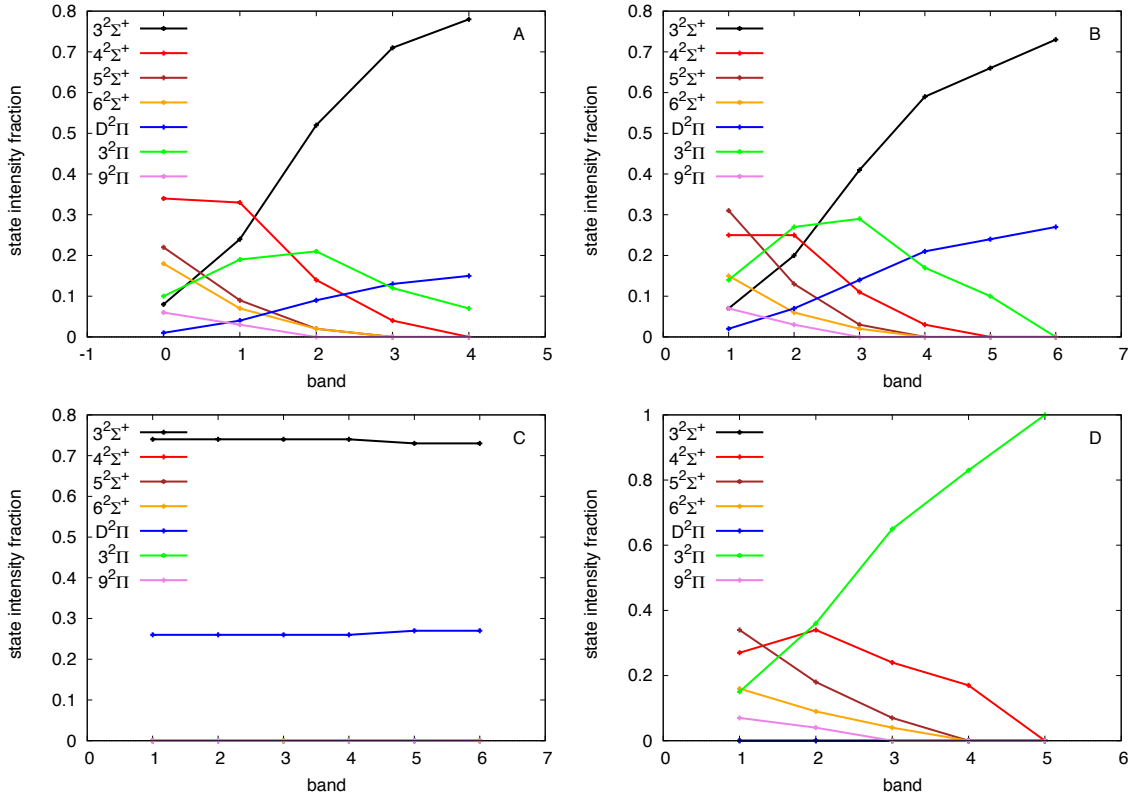

Fig. S16. Relative contributions of states to RABBITT sidebands. (**A**) CO axis is parallel to the polarization. (**B**) CO axis is perpendicular to the polarization. Note that sideband 0 in the parallel orientation is not measured in the experiment. CO axis is perpendicular to the polarization selected on (**C**) low KER. (**D**) high KER.

Fig. S17.

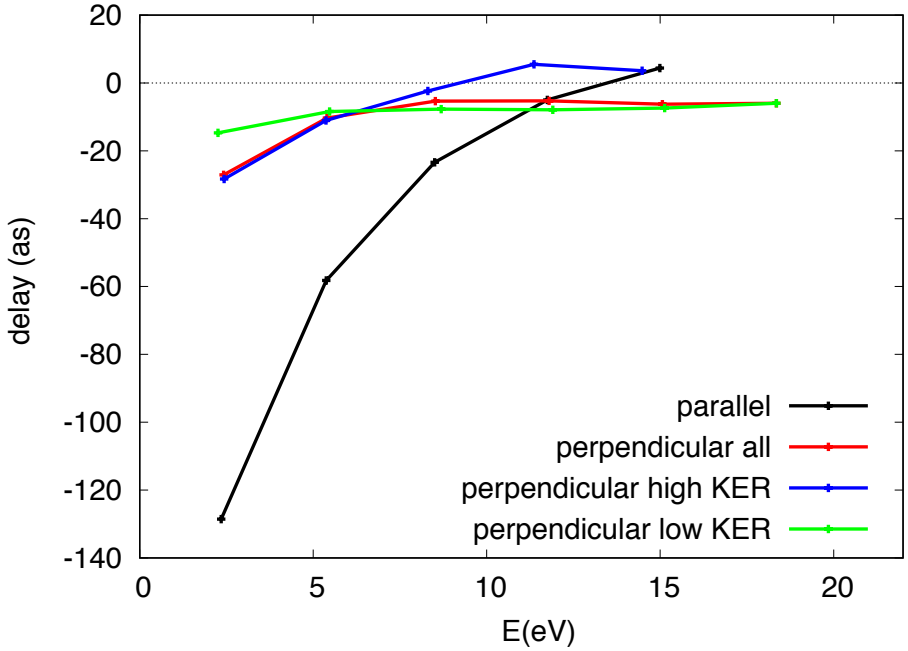

Fig. S17. Simulated state-integrated stereo-photoionization delays of CO.

Fig. S18.

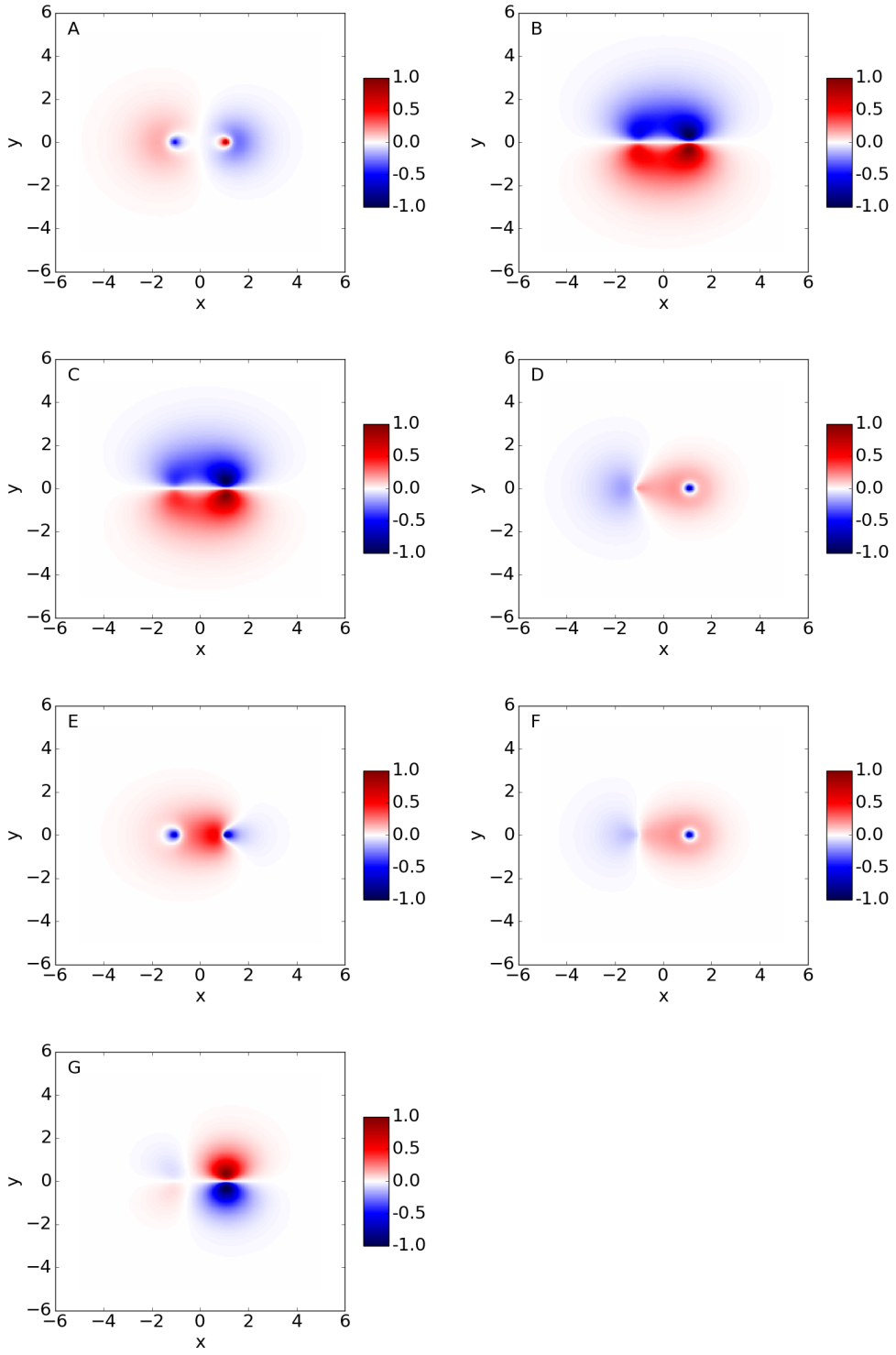

Fig. S18. DOs in the position space. The following states are represented: $\mathbf{3^2\Sigma^+}$ (**A**), $\mathbf{D^2\Pi}$ (**B**), $\mathbf{3^2\Pi}$ (**C**), $\mathbf{4^2\Sigma^+}$ (**D**), $\mathbf{5^2\Sigma^+}$ (**E**), $\mathbf{6^2\Sigma^+}$ (**F**) and $\mathbf{9^2\Pi}$ (**G**) with C(x)=-1.07 au, O(y)=1.07 au. (Color scale is arbitrary.)

Fig. S19.

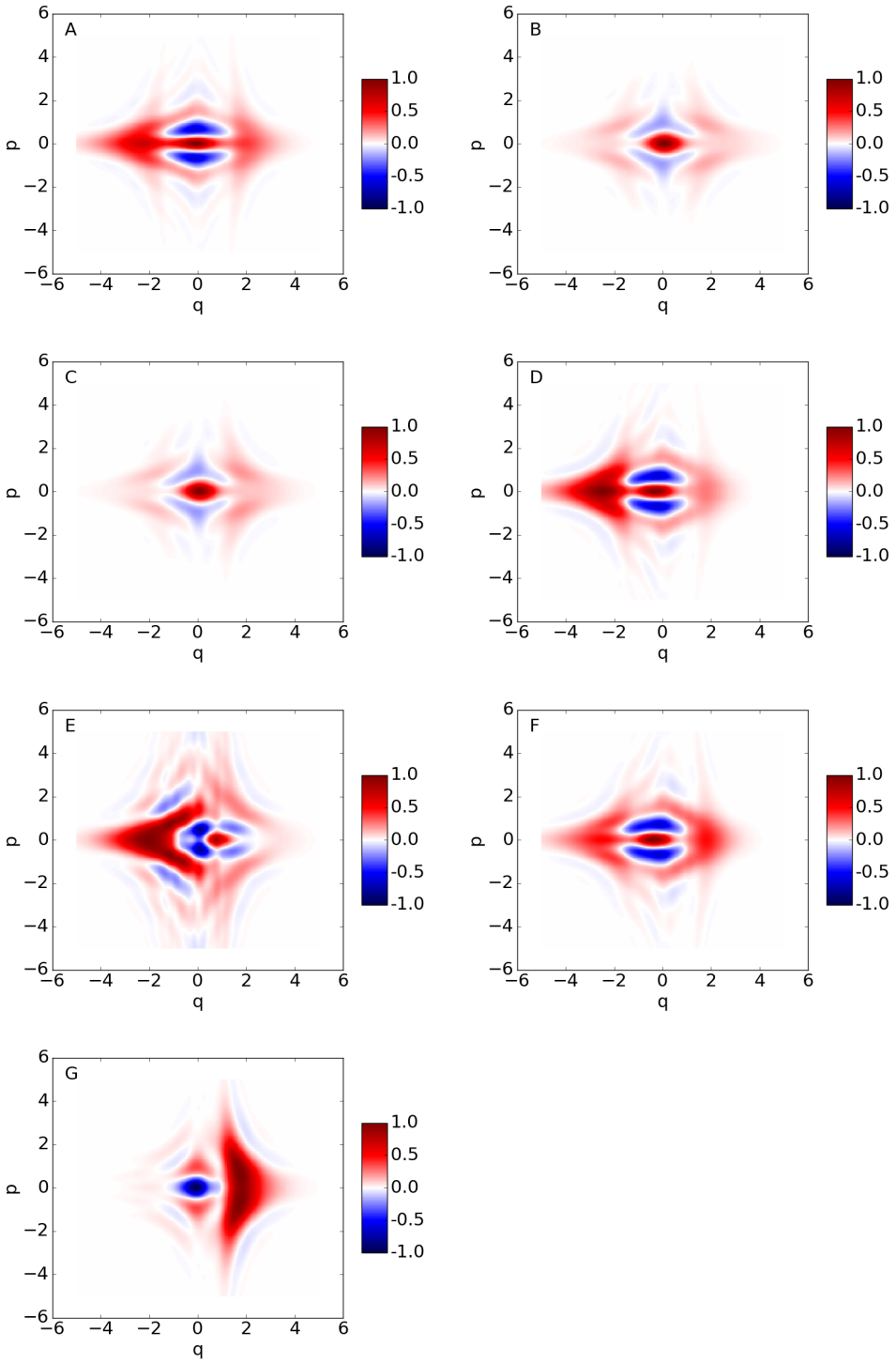

Fig. S19. 2-D phase-space cut of Wigner functions of DTMs of $3^2\Sigma^+$ (A), $D^2\Pi$ (B), $3^2\Pi$ (C), $4^2\Sigma^+$ (D), $5^2\Sigma^+$ (E), $6^2\Sigma^+$ (F) and $9^2\Pi$ (G) states. The field is oriented parallel to the molecular axis. For Σ states, the cut passes through the molecular axis (in both position and momentum space). For $^2\Pi$ states, which have the node along the molecular axis, the cut is inclined from the molecular axis by 30 degrees. C(q)=-1.07 au, O(q)=1.07 au. (Color scale is arbitrary.)

Fig. S20.

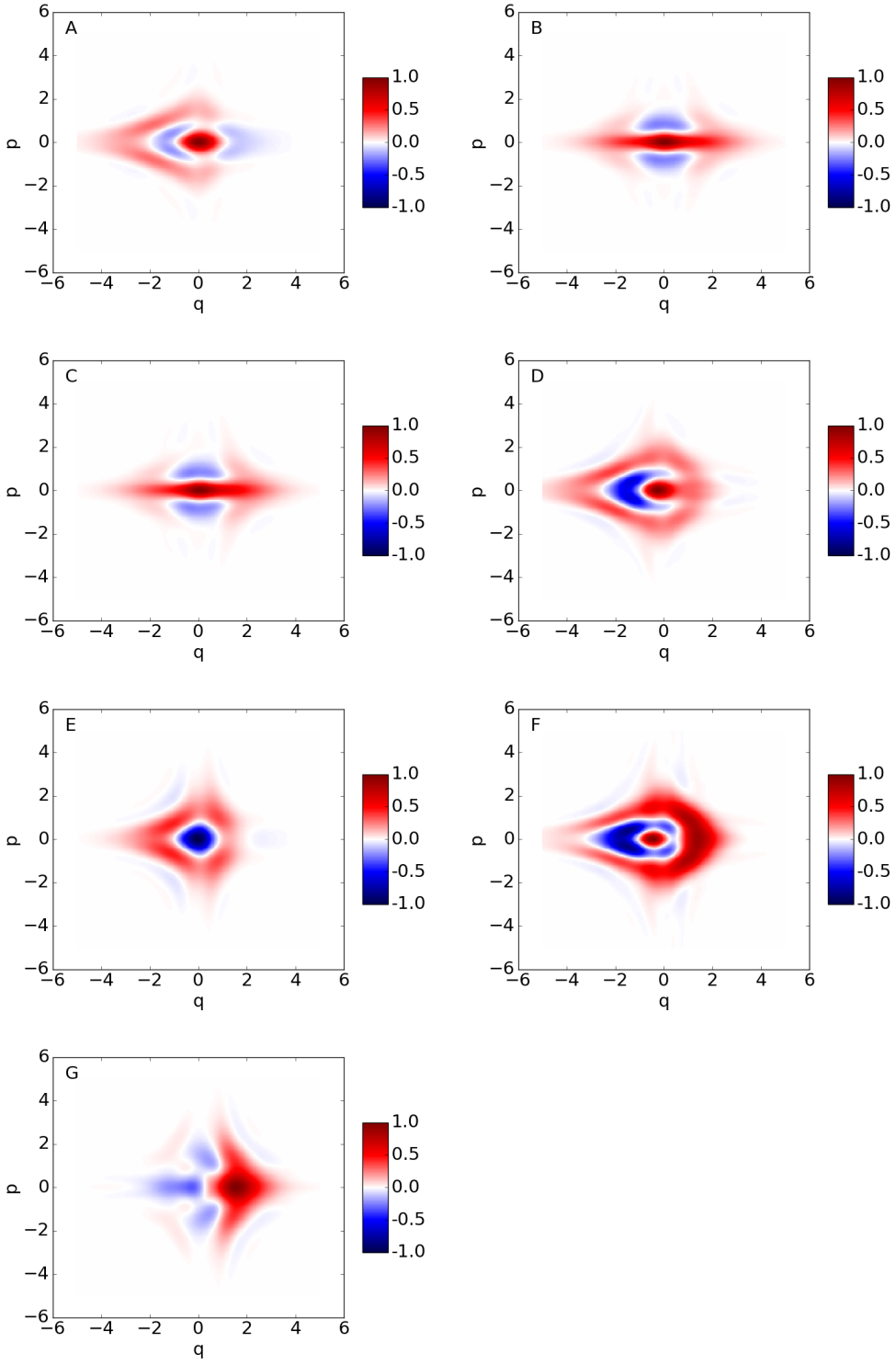

Fig. S20. 2-D phase-space cut of Wigner functions of DTMs of $3^2\Sigma^+$ (A), $D^2\Pi$ (B), $3^2\Pi$ (C), $4^2\Sigma^+$ (D), $5^2\Sigma^+$ (E), $6^2\Sigma^+$ (F) and $9^2\Pi$ (G). The field is oriented perpendicular to the molecular axis and the cut is inclined from the direction perpendicular to the molecular axis by 30 degrees (in both position and momentum space). C(q)=-1.07 au, O(q)=1.07 au. (Color scale is arbitrary.)

Fig. S21.

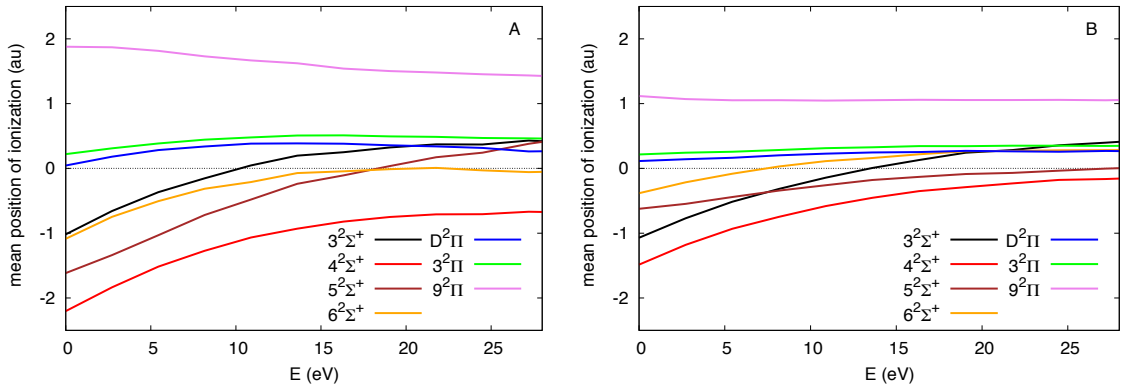

Fig. S21 Energy-dependent mean position of the electron at the time of ionization. The position is measured on the molecular axis with the position zero being located exactly in the middle between carbon and oxygen. The carbon atom is located at -1.07 au whereas oxygen at 1.07 au. (**A**) CO axis is parallel to the polarization. (**B**) CO axis is perpendicular to the polarization.

Fig. S22.

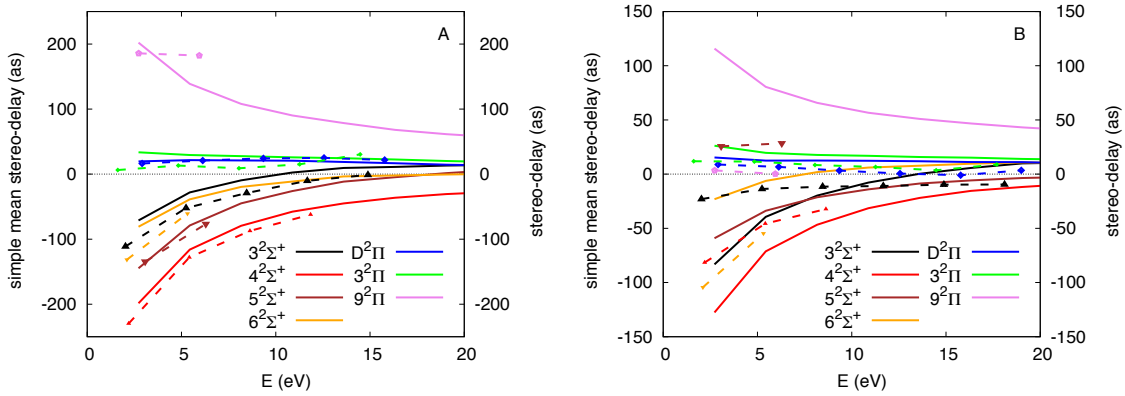

Fig. S22. Comparison of the energy-dependent stereo-photoionization delays (dashed lines) with simple mean stereo-delay position (solid lines). (**A**) CO axis is parallel to the polarization. (**B**) CO axis is perpendicular to the polarization.

Fig. S23.

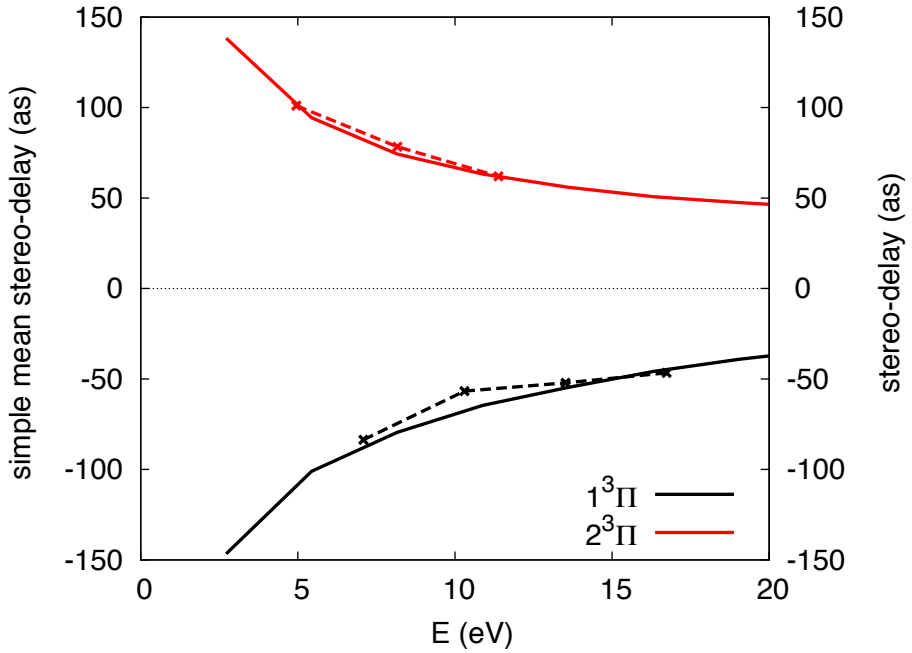

Fig. S23. Comparison of the energy-dependent stereo-photoionization delays (dashed lines) with the simple mean stereo-delay position (solid lines) for the 2 lowest electronic states $^3\Pi$ of NO.

Fig. S24.

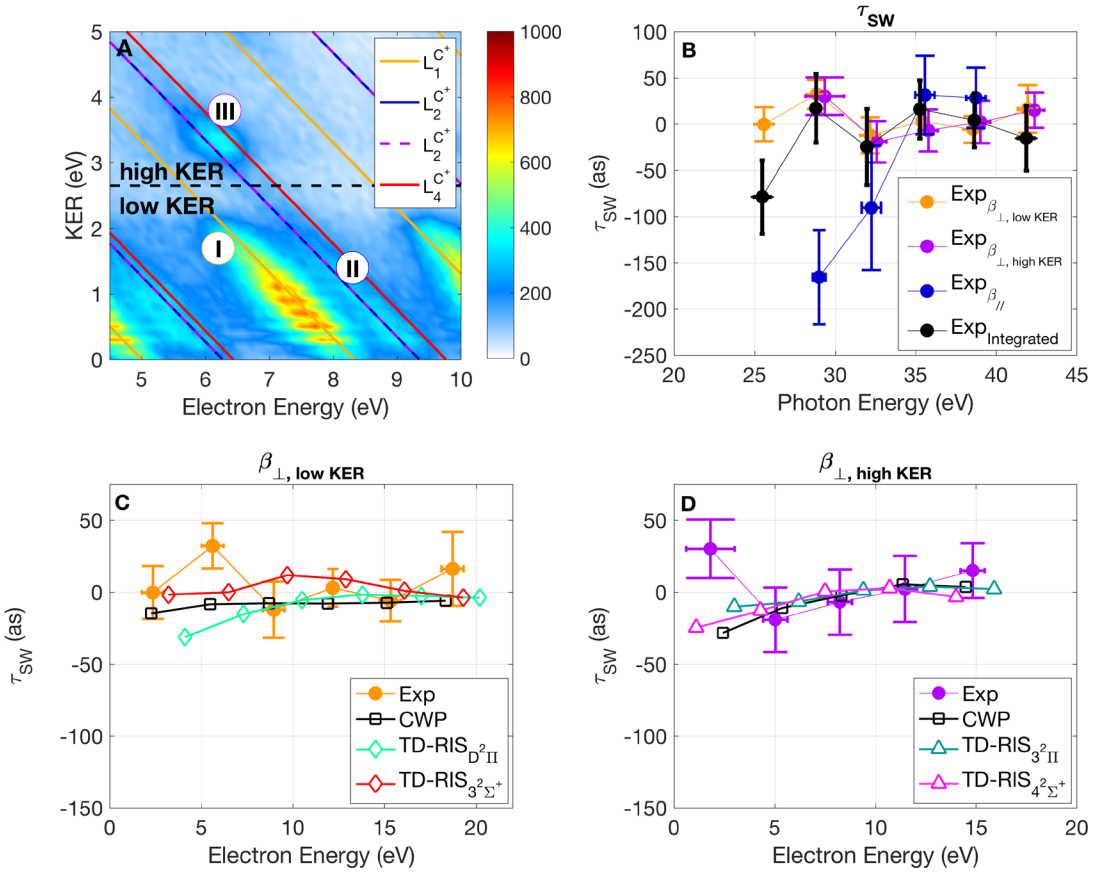

Fig. S24. Stereo Wigner Time delay (SWTD) for perpendicular orientation. (**A**) The Kinetic Energy Correlation Diagram (KECD) shows the correlated Kinetic Energy Release (KER) and electron energy ($\boldsymbol{C^+ + O, e^-}$), which uniquely defines the reaction pathway. The dissociation limits $\boldsymbol{L_1^{C^+}}$, $\boldsymbol{L_2^{C^+}}$ and $\boldsymbol{L_4^{C^+}}$ are indicated by the orange solid, blue/purple dashed and red solid lines, respectively. Simulation of dissociation dynamics shows that whereas in the adiabatic approximation the $\boldsymbol{4^2\Sigma^+}$-state dissociates solely towards $\boldsymbol{L_1^{O^+}}$ (dark red curve in (A)), it dissociates towards several limits including $\boldsymbol{L_4^{C^+}}$ (red diagonal lines in (B)) in a more complete model including nonadiabatic couplings. Apart from $\boldsymbol{3^2\Sigma^+}$, all $\boldsymbol{\Sigma}$- and $\boldsymbol{\Pi}$-states dissociate nonadiabatically along multiple PES. Fine structure in the low KER region arises from the vibrational progression in the final state along which the molecule evolves and dissociates. (**B**) The SWTDs are shown for those photoelectrons in coincidence with the perpendicular (with respect to the laser polarization axis) and parallel oriented recoil fragment ion. The two distinct contributions in perpendicular orientation are selected according to the Kinetic Energy Release (KER) distribution (see Fig. 1B). We also compare theory and experiment in perpendicular orientation for the low KER selected photoelectrons in (**C**) and the high KER selected photoelectrons in (**D**).

Table S1. Summary of the calculated doublet states of CO^+ (R = 1.128323 Å)

State	I_p, eV*	Expt.†	$\|\psi_D\|^2$‡	Fragment§	Channel**	Remarks
$X\ 1^2\Sigma^+$	14.014	14.0	0.8790	CO^+	1	
$A\ 1^2\Pi$	16.948	16.9	0.8748	CO^+	2††, 3‡‡	
$B\ 2^2\Sigma^+$	19.675	19.7	0.7851	CO^+	4	
$D\ 2^2\Pi$	23.228	22.7	0.0072	CO^+	5††, 6‡‡	Onset of C^+ at higher energies
$1^2\Sigma^-$	23.406		0.0000	C^+		Forbidden
$1^2\Delta$	23.503		0.0003	C^+	7§§, 8***	
$C\ 3^2\Sigma^+$	24.108	23.4	0.0910	CO+	9	Long-lived predissociative state
$2^2\Delta$	25.577	25.3	0.0004	C^+	10§§, 11***	
$2^2\Sigma^-$	26.186		0.0000	C^+		Forbidden
$3^2\Pi$	27.552	27.5	0.0064	C^+	12††, 13‡‡	
$4^2\Pi$	28.107	28.2	0.0059	C^+	14††, 15‡‡	
$5^2\Pi$	28.653	28.5	0.0038	C^+	16††, 17‡‡	
$1^2\Phi$	28.932		0.0000	C^+		Cross-section too low to contribute
$4^2\Sigma^+$	29.467	29.0	0.0272	O^+	18	Onset of the O^+ fragment channel

* Calculated vertical I_p + 0.944 eV (see text)
† Experimental vertical I_p, cited from *(38)*
‡ Squared norm of the Dyson orbital
§ Dominant ion product, based on *(31)*
** Channel number in TD-RIS calculation
†† B_1 irreducible representation in the C_{2v} subgroup
‡‡ B_2 irreducible representation in the C_{2v} subgroup
§§ A_1 irreducible representation in the C_{2v} subgroup
*** A_2 irreducible representation in the C_{2v} subgroup

Table S2. Summary of the single-harmonic XUV pulses

Harmonic	$\hbar\Omega$, eV	Delay, as	Weight
15	24.12	0.0	0.075
17	27.34	74.0	0.303
19	30.55	147.9	0.670
21	33.77	221.9	1.000
23	36.99	295.9	0.409
25	40.20	369.9	0.074
27	43.42	443.8	0.018

Table S3. TD-RIS ion-state resolved directional time delays for single-harmonic pulses.

H*	E, eV†	$\boldsymbol{\Delta T}_{\|\|}$, as‡	$Y_{\|\|}(O)$§	$Y_{\|\|}(C)$**	$\boldsymbol{\Delta T}_{\perp}$,as††	$Y_{\perp}(O)$‡‡	$Y_{\perp}(C)$§§
$X\ 1^2\Sigma^+$							
H15	10.1	†††††	2332	4642	-8	6096	7937
H17	13.3	-27	1294	3036	-7	3901	5324
H19	16.5	-19	1039	2231	-9	2952	4060
H21	19.8	-22	893	1682	-12	2365	3262
H23	23.0	-22	705	1198	-13	1852	2641
H25	26.2	-23	476	758	-12	1352	2043
H27	29.4	-23	291	453	-9	970	1572
$A\ 1^2\Pi$							
H15	7.2	†††††	2410	1552	-10	12975	13618
H17	10.4	-6	592	672	5	8530	9695
H19	13.6	-3	347	408	3	6502	7447
H21	16.8	1	267	289	4	5038	5833
H23	20.0	2	224	217	3	3961	4560
H25	23.3	2	190	169	1	3163	3588
H27	26.5	4	160	135	1	2538	2855
$B\ 2^2\Sigma^+$							
H15	4.5	-11	1809	1437	19	4347	4085
H17	7.7	20	547	584	-10	1530	1664
H19	10.9	48	317	346	15	980	1063
H21	14.1	37	348	292	14	1051	970
H23	17.3	25	411	277	15	1174	947
H25	20.5	19	417	254	16	1220	867
H27	23.7	15	356	209	13	1169	728
$D\ 2^2\Pi$							
H15	0.9	†††††	52	56	***	205	201
H17	4.1	-77	28	38	-31	150	139
H19	7.3	17	13	26	-15	89	89
H21	10.5	29	9	19	-6	60	69
H23	13.8	19	6	13	-2	43	55
H25	17.0	8	5	8	-3	32	43
H27	20.2	1	3	5	-4	24	34

* Harmonic number. See Table S2 for the pulse parameters

† Central photoelectron energy in electron-Volts

‡ Time Delay for photoelectrons arriving at the oxygen-side detector relative to the carbon-end detector in attoseconds, molecular axis oriented parallel to the polarization direction (Eqs. S3-S4)

§ Total number of photoelectrons per CO molecule arriving at the oxygen-side detector, times 10^8, molecular axis parallel to the field polarization (Eq. S3).

** Total number of photoelectrons per CO molecule arriving at the oxygen-carbon detector, times 10^8, molecular axis parallel to the field orientation (Eq. S4).

†† Time Delay for photoelectrons arriving at the oxygen-side detector relative to the carbon-end detector in attoseconds, molecular axis oriented perpendicular to the field polarization (Eqs. S5-S6).

‡‡ Total number of photoelectrons per CO molecule arriving at the oxygen-side detector, times 10^8, molecular axis perpendicular to the field polarization (Eq. S5).

§§ Total number of photoelectrons per CO molecule arriving at the oxygen-carbon detector, times 10^8, molecular axis perpendicular to the field polarization (Eq. S6).

*** The delay cannot be determined, see text.

$1^2\Delta$							
H15	0.6	-105	4	5	-98	29	34
H17	3.8	-112	5	6	-72	25	38
H19	7.1	-38	3	5	-19	12	21
H21	10.3	-13	2	4	-6	8	13
H23	13.5	-17	1	3	-6	5	8
H25	16.7	-18	1	2	-8	4	6
H27	19.9	-19	0	1	-7	3	4
$C\ 3^2\Sigma^+$							
H17	3.2	-77	194	363	-2	757	944
H19	6.5	-35	90	211	-0	307	362
H21	9.7	-17	45	124	12	110	127
H23	12.9	-15	30	89	9	61	69
H25	16.1	-11	23	74	1	48	54
H27	19.3	-7	19	63	-4	43	49
2Δ							
H17	1.8	52	8	8	77	87	110
H19	5.0	6	9	8	8	80	77
H21	8.2	-9	8	7	-10	51	49
H23	11.4	-2	7	6	-5	33	35
H25	14.6	2	6	6	-1	23	26
H27	17.8	2	4	5	1	17	20
$3^2\Pi$							
H19	3.0	0	16	25	-10	60	110
H21	6.2	8	15	23	-7	57	96
H23	9.4	15	11	16	1	46	73
H25	12.7	19	7	11	4	38	57
H27	15.9	17	5	7	2	32	45
$4^2\Pi$							
H19	2.5	-26	57	58	-25	113	137
H21	5.7	-19	45	53	-24	90	106
H23	8.9	-12	25	33	-15	53	65
H25	12.1	-14	13	20	-12	33	41
H27	15.3	-20	7	12	-13	22	27
$5^2\Pi$							
H19	1.9	73	39	41	21	409	199
H21	5.1	53	34	32	20	340	165
H23	8.3	26	23	20	11	221	108
H25	11.6	25	17	17	7	155	81
H27	14.8	25	13	15	11	117	71
$4^2\Sigma^+$							
H19	1.1	-69	73	188	-25	293	463
H21	4.3	-61	59	158	-13	238	370
H23	7.5	-31	30	98	0	114	173
H25	10.7	-1	21	80	3	70	97
H27	14.0	2	21	75	-3	56	68

Table S4. Ionization potentials (IPs) and spectroscopic intensity factors (SIFs)

State	$3^2\Sigma^+$	$4^2\Sigma^+$	$5^2\Sigma^+$	$6^2\Sigma^+$	$D^2\Pi$	$3^2\Pi$	$9^2\Pi$
I_p (eV)	23.70	29.96	32.31	33.27	22.82	27.33	32.65
SIF	0.0932	0.0313	0.0871	0.0225	0.0049	0.0096	0.0244

Table S5. Dipole moments computed with MR-CIS. Negative dipole moments point towards carbon. The dipole moments were computed in the geometric center of the molecule exactly in the middle between carbon and oxygen.

State	$3^2\Sigma^+$	$4^2\Sigma^+$	$5^2\Sigma^+$	$6^2\Sigma^+$	$D^2\Pi$	$3^2\Pi$	$9^2\Pi$
Dipole (a.u.)	-0.34	-0.03	0.59	0.15	-0.63	-0.08	0.36

Table S6. Mean positions of the electron along the molecular axis computed with MR-CIS. The carbon atom is located at -1.07 au whereas oxygen at 1.07 au.

State	$3^2\Sigma^+$	$4^2\Sigma^+$	$5^2\Sigma^+$	$6^2\Sigma^+$	$D^2\Pi$	$3^2\Pi$	$9^2\Pi$
DO $\langle q \rangle$ (a.u.)	-0.07	-0.33	0.03	0.36	0.23	0.42	1.07
Parallel DTM $\langle q \rangle$ (a.u.)	-0.80	-1.65	-0.94	-0.47	0.10	0.43	1.43
Perpendicular DTM $\langle q \rangle$ (a.u.)	-0.70	-0.94	-0.28	0.10	0.15	0.29	1.11

Table S7. Axial recoil approximation: asymptotic dissociation kinetic energies used in the calculation of the rotation angle **θ.**

State	$3\,^2\Sigma^+$	$D\,^2\Pi$	$3\,^2\Pi$	$4\,^2\Sigma^+$	$5\,^2\Sigma^+$	$6\,^2\Sigma^+$
E_c(eV)	0.243	0.39	3.3	2.2	4.0	5.2

Table S8. **Axial recoil approximation:** times after ionization t_c to reach nuclear separation $r_c = 10$ au.

State	$3\,^2\Sigma^+$	$D\,^2\Pi$	$3\,^2\Pi$	$4\,^2\Sigma^+$	$5\,^2\Sigma^+$	$6\,^2\Sigma^+$
t_c(fs)	180	2000	96	56	43	40

Table S9. **Axial recoil approximation**: angles of rotation θ of the molecular axis after ionization.

State	$3\,^2\Sigma^+$	$D\,^2\Pi$	$3\,^2\Pi$	$4\,^2\Sigma^+$	$5\,^2\Sigma^+$	$6\,^2\Sigma^+$
θ(deg)	3.4	70.2	1.3	1.1	0.8	0.8

References and Notes

1. K. Klünder, J. M. Dahlström, M. Gisselbrecht, T. Fordell, M. Swoboda, D. Guénot, P. Johnsson, J. Caillat, J. Mauritsson, A. Maquet, R. Taïeb, A. L'Huillier, Probing single-photon ionization on the attosecond time scale. *Phys. Rev. Lett.* **106**, 143002 (2011). doi:10.1103/PhysRevLett.106.143002 Medline

2. M. Schultze, M. Fiess, N. Karpowicz, J. Gagnon, M. Korbman, M. Hofstetter, S. Neppl, A. L. Cavalieri, Y. Komninos, T. Mercouris, C. A. Nicolaides, R. Pazourek, S. Nagele, J. Feist, J. Burgdörfer, A. M. Azzeer, R. Ernstorfer, R. Kienberger, U. Kleineberg, E. Goulielmakis, F. Krausz, V. S. Yakovlev, Delay in photoemission. *Science* **328**, 1658–1662 (2010). doi:10.1126/science.1189401 Medline

3. L. Cattaneo, J. Vos, M. Lucchini, L. Gallmann, C. Cirelli, U. Keller, Comparison of attosecond streaking and RABBITT. *Opt. Express* **24**, 29060–29076 (2016). doi:10.1364/OE.24.029060 Medline

4. M. Sabbar, S. Heuser, R. Boge, M. Lucchini, T. Carette, E. Lindroth, L. Gallmann, C. Cirelli, U. Keller, Resonance effects in photoemission time delays. *Phys. Rev. Lett.* **115**, 133001 (2015). doi:10.1103/PhysRevLett.115.133001 Medline

5. E. P. Wigner, Lower limit for the energy derivative of the scattering phase shift. *Phys. Rev.* **98**, 145–147 (1955). doi:10.1103/PhysRev.98.145

6. R. Pazourek, S. Nagele, J. Burgdörfer, Attosecond chronoscopy of photoemission. *Rev. Mod. Phys.* **87**, 765–802 (2015). doi:10.1103/RevModPhys.87.765

7. M. Huppert, I. Jordan, D. Baykusheva, A. von Conta, H. J. Wörner, Attosecond delays in molecular photoionization. *Phys. Rev. Lett.* **117**, 093001 (2016). doi:10.1103/PhysRevLett.117.093001 Medline

8. S. Haessler, B. Fabre, J. Higuet, J. Caillat, T. Ruchon, P. Breger, B. Carré, E. Constant, A. Maquet, E. Mével, P. Salières, R. Taïeb, Y. Mairesse, Phase-resolved attosecond near-threshold photoionization of molecular nitrogen. *Phys. Rev. A* **80**, 011404 (2009). doi:10.1103/PhysRevA.80.011404

9. L. Cattaneo, J. Vos, R. Y. Bello, A. Palacios, S. Heuser, L. Pedrelli, M. Lucchini, C. Cirelli, F. Martín, U. Keller, Attosecond coupled electron and nuclear dynamics in dissociative ionization of H_2. *Nat. Phys.* 10.1038/s41567-018-0103-2 (2018). doi:10.1038/s41567-018-0103-2

10. C. Marceau, V. Makhija, D. Platzer, A. Y. Naumov, P. B. Corkum, A. Stolow, D. M. Villeneuve, P. Hockett, Molecular frame reconstruction using time-domain photoionization interferometry. *Phys. Rev. Lett.* **119**, 083401 (2017). doi:10.1103/PhysRevLett.119.083401 Medline

11. P. Hockett, E. Frumker, D. M. Villeneuve, P. B. Corkum, Time delay in molecular photoionization. *J. Phys. B At. Mol. Opt. Phys.* **49**, 095602 (2016). doi:10.1088/0953-4075/49/9/095602

12. I. A. Ivanov, A. S. Kheifets, V. V. Serov, Attosecond time-delay spectroscopy of the hydrogen molecule. *Phys. Rev. A* **86**, 063422 (2012). doi:10.1103/PhysRevA.86.063422

13. V. V. Serov, V. L. Derbov, T. Sergeeva, Interpretation of time delay in the ionization of two-center systems. *Phys. Rev. A* **87**, 063414 (2013). doi:10.1103/PhysRevA.87.063414

14. V. V. Serov, A. S. Kheifets, Time delay in XUV/IR photoionization of H_2O. *J. Chem. Phys.* **147**, 204303 (2017). doi:10.1063/1.4993493 Medline

15. P. Hockett, Angle-resolved RABBITT: Theory and numerics. *J. Phys. B At. Mol. Opt. Phys.* **50**, 154002 (2017). doi:10.1088/1361-6455/aa7887

16. G. Sansone, F. Kelkensberg, J. F. Pérez-Torres, F. Morales, M. F. Kling, W. Siu, O. Ghafur, P. Johnsson, M. Swoboda, E. Benedetti, F. Ferrari, F. Lépine, J. L. Sanz-Vicario, S. Zherebtsov, I. Znakovskaya, A. L'huillier, M. Y. Ivanov, M. Nisoli, F. Martín, M. J. J. Vrakking, Electron localization following attosecond molecular photoionization. *Nature* **465**, 763–766 (2010). doi:10.1038/nature09084 Medline

17. Ch. Neidel, J. Klei, C.-H. Yang, A. Rouzée, M. J. J. Vrakking, K. Klünder, M. Miranda, C. L. Arnold, T. Fordell, A. L'Huillier, M. Gisselbrecht, P. Johnsson, M. P. Dinh, E. Suraud, P.-G. Reinhard, V. Despré, M. A. L. Marques, F. Lépine, Probing time-dependent molecular dipoles on the attosecond time scale. *Phys. Rev. Lett.* **111**, 033001 (2013). doi:10.1103/PhysRevLett.111.033001 Medline

18. C. Cirelli, C. Marante, S. Heuser, C. L. M. Petersson, Á. J. Galán, L. Argenti, S. Zhong, D. Busto, M. Isinger, S. Nandi, S. Maclot, L. Rading, P. Johnsson, M. Gisselbrecht, M. Lucchini, L. Gallmann, J. M. Dahlström, E. Lindroth, A. L'Huillier, F. Martín, U. Keller, Anisotropic photoemission time delays close to a Fano resonance. *Nat. Commun.* **9**, 955 (2018). doi:10.1038/s41467-018-03009-1 Medline

19. S. Heuser, Á. Jiménez Galán, C. Cirelli, C. Marante, M. Sabbar, R. Boge, M. Lucchini, L. Gallmann, I. Ivanov, A. S. Kheifets, J. M. Dahlström, E. Lindroth, L. Argenti, F. Martín, U. Keller, Angular dependence of photoemission time delay in helium. *Phys. Rev. A* **94**, 063409 (2016). doi:10.1103/PhysRevA.94.063409

20. A. Chacon, M. Lein, C. Ruiz, Asymmetry of Wigner's time delay in a small molecule. *Phys. Rev. A* **89**, 053427 (2014). doi:10.1103/PhysRevA.89.053427

21. J. H. D. Eland, E. J. Duerr, Dissociation and electron-ion angular distributions in inner-valence photoionisation of CO and N_2. *Chem. Phys.* **229**, 13–19 (1998). doi:10.1016/S0301-0104(97)00332-7

22. M. Lebech, J. C. Houver, D. Dowek, Valence and inner-valence shell dissociative photoionization of CO in the 26-33 eV range. I. Ion-electron kinetic energy correlation and laboratory frame photoemission. *J. Chem. Phys.* **130**, 194307 (2009). doi:10.1063/1.3125223 Medline

23. M. Lebech, J. C. Houver, G. Raseev, A. S. dos Santos, D. Dowek, R. R. Lucchese, Valence and inner-valence shell dissociative photoionization of CO in the 26-33 eV range. II. Molecular-frame and recoil-frame photoelectron angular distributions. *J. Chem. Phys.* **136**, 094303 (2012). doi:10.1063/1.3681920 Medline

24. R. Dörner, V. Mergel, O. Jagutzki, L. Spielberger, J. Ullrich, R. Moshammer, H. Schmidt-Böcking, Cold target recoil ion momentum spectroscopy: A 'momentum microscope' to view atomic collision dynamics. *Phys. Rep.* **330**, 95–192 (2000). doi:10.1016/S0370-1573(99)00109-X

25. J. Ullrich, R. Moshammer, A. Dorn, R. Dörner, L. P. H. Schmidt, H. Schmidt-Böcking, Recoil-ion and electron momentum spectroscopy: Reaction-microscopes. *Rep. Prog. Phys.* **66**, 1463–1545 (2003). doi:10.1088/0034-4885/66/9/203

26. P. M. Paul, E. S. Toma, P. Breger, G. Mullot, F. Auge, P. Balcou, H. G. Muller, P. Agostini, Observation of a train of attosecond pulses from high harmonic generation. *Science* **292**, 1689–1692 (2001). doi:10.1126/science.1059413 Medline

27. H. G. Muller, Reconstruction of attosecond harmonic beating by interference of two-photon transitions. *Appl. Phys. B* **74**, s17–s21 (2014). doi:10.1007/s00340-002-0894-8

28. R. N. Zare, Photoejection dynamics. *Mol. Photochem.* **4**, 1–37 (1972).

29. M. Lebech, J. C. Houver, A. Lafosse, D. Dowek, C. Alcaraz, L. Nahon, R. R. Lucchese, Complete description of linear molecule photoionization achieved by vector correlations using the light of a single circular polarization. *J. Chem. Phys.* **118**, 9653–9663 (2003). doi:10.1063/1.1570402

30. A. Lafosse, M. Lebech, J. C. Brenot, P. M. Guyon, O. Jagutzki, L. Spielberger, M. Vervloet, J. C. Houver, D. Dowek, Vector correlations in dissociative photoionization of diatomic molecules in the VUV range: Strong anisotropies in electron emission from spatially oriented NO molecules. *Phys. Rev. Lett.* **84**, 5987–5990 (2000). doi:10.1103/PhysRevLett.84.5987 Medline

31. P. Baltzer, M. Lundqvist, B. Wannberg, L. Karlsson, M. Larsson, M. A. Hayes, J. B. West, M. R. F. Siggel, A. C. Parr, J. L. Dehmer, Inner-valence states of CO^+ between 22 eV and 46 eV studied by high resolution photoelectron spectroscopy and *ab initio* CI calculations. *J. Phys. B At. Mol. Opt. Phys.* **27**, 4915–4932 (1994). doi:10.1088/0953-4075/27/20/011

32. J. M. Dahlström, A. L'Huillier, A. Maquet, Introduction to attosecond delays in photoionization. *J. Phys. B At. Mol. Opt. Phys.* **45**, 183001 (2012). doi:10.1088/0953-4075/45/18/183001

33. M. Spanner, S. Patchkovskii, One-electron ionization of multielectron systems in strong nonresonant laser fields. *Phys. Rev. A* **80**, 063411 (2009). doi:10.1103/PhysRevA.80.063411

34. M. Spanner, S. Patchkovskii, Molecular strong field ionization and high harmonic generation: A selection of computational illustrations. *Chem. Phys.* **414**, 10–19 (2013). doi:10.1016/j.chemphys.2011.12.016

35. A. E. Boguslavskiy, J. Mikosch, A. Gijsbertsen, M. Spanner, S. Patchkovskii, N. Gador, M. J. J. Vrakking, A. Stolow, The multielectron ionization dynamics underlying attosecond strong-field spectroscopies. *Science* **335**, 1336–1340 (2012). doi:10.1126/science.1212896 Medline

36. J. Vos, Orientation-dependent stereo Wigner time delay and electron localization in a small molecule, Research Collection ETH Zurich (2018); doi:10.3929/ethz-b-000259345.

37. M. Sabbar, S. Heuser, R. Boge, M. Lucchini, L. Gallmann, C. Cirelli, U. Keller, Combining attosecond XUV pulses with coincidence spectroscopy. *Rev. Sci. Instrum.* **85**, 103113 (2014). doi:10.1063/1.4898017 Medline

38. R. A. Kendall, T. H. Dunning Jr., R. J. Harrison, Electron affinities of the first-row atoms revisited. Systematic basis sets and wave functions. *J. Chem. Phys.* **96**, 6796–6806 (1992). doi:10.1063/1.462569

39. G. Herzberg, K. P. Huber, *Molecular Spectra and Molecular Structure: Constants of Diatomic Molecules* (Van Nostrand Reinhold, 1979).

40. A. Bergner, M. Dolg, W. Küchle, H. Stoll, H. Preuß, Ab initio energy-adjusted pseudopotentials for elements of groups 13–17. *Mol. Phys.* **80**, 1431–1441 (1993). doi:10.1080/00268979300103121

41. D. E. Manolopoulos, Derivation and reflection properties of a transmission-free absorbing potential. *J. Chem. Phys.* **117**, 9552–9559 (2002). doi:10.1063/1.1517042

42. S. Patchkovskii, Z. Zhao, T. Brabec, D. M. Villeneuve, High harmonic generation and molecular orbital tomography in multielectron systems. *J. Chem. Phys.* **126**, 114306 (2007). doi:10.1063/1.2711809 Medline

43. D. A. Varshalovich, A. N. Moskalev, V. K. Khersonskii, *Quantum Theory of Angular Momentum* (World Scientific, 1988).

44. E. J. Heller, Phase space interpretation of semiclassical theory. *J. Chem. Phys.* **67**, 3339–3351 (1977). doi:10.1063/1.435296

45. H. Wang, X. Sun, W. H. Miller, Semiclassical approximations for the calculation of thermal rate constants for chemical reactions in complex molecular systems. *J. Chem. Phys.* **108**, 9726–9736 (1998). doi:10.1063/1.476447

46. National Institute of Standards and Technology (NIST), Computational Chemistry Comparison and Benchmark DataBase, R. D. Johnson III, Ed. (NIST Standard Reference Database 101); http://cccbdb.nist.gov/.

47. M. W. Schmidt, K. K. Baldridge, J. A. Boatz, S. T. Elbert, M. S. Gordon, J. H. Jensen, S. Koseki, N. Matsunaga, K. A. Nguyen, S. Su, T. L. Windus, M. Dupuis, J. A. Montgomery, General atomic and molecular electronic structure system. *J. Comput. Chem.* **14**, 1347–1363 (1993). doi:10.1002/jcc.540141112

48. S. Patchkovskii, Z. Zhao, T. Brabec, D. M. Villeneuve, High harmonic generation and molecular orbital tomography in multielectron systems: Beyond the single active electron approximation. *Phys. Rev. Lett.* **97**, 123003 (2006). doi:10.1103/PhysRevLett.97.123003 Medline

49. T. Zimmermann, L. Ortmann, C. Hofmann, J. M. Rost, A. S. Landsman, Attosecond streaking delays in multi-electron systems. arXiv:1804.09583 [physics.chem-ph] (25 April 2018).

50. J. M. Dahlström, D. Guénot, K. Klünder, M. Gisselbrecht, J. Mauritsson, A. L'Huillier, A. Maquet, R. Taïeb, Theory of attosecond delays in laser-assisted

photoionization. *Chem. Phys.* **414**, 53–64 (2013). doi:10.1016/j.chemphys.2012.01.017

51. H.-J. Werner, P. J. Knowles, G. Knizia, F. R. Manby, M. Schutz, P. Celani, T. Korona, R. Lindh, A. Mitrushenkov, G. Rauhut, K. R. Shamasundar, T. B. Adler, R. D. Amos, A. Bernhardsson, A. Berning, D. L. Cooper, M. J. O. Deegan, A. J. Dobbyn, F. Eckert, E. Goll, C. Hampel, A. Hesselmann, G. Hetzer, T. Hrenar, G. Jansen, C. Koppl, Y. Liu, A. W. Lloyd, R. A. Mata, A. J. May, S. J. McNicholas, W. Meyer, M. E. Mura, A. Nicklass, D. P. O'Neill, P. Palmieri, K. Pfluger, R. Pitzer, M. Reiher, T. Shiozaki, H. Stoll, A. J. Stone, R. Tarroni, T. Thorsteinsson, M. Wang, A. Wolf, MOLPRO, version 2010.1, a package of *ab initio* programs (Molpro, 2010); http://www.molpro.net/.

52. D. Kosloff, R. Kosloff, A Fourier method solution for a time dependent Schrödinger equation as a tool in molecular dynamics. *J. Comput. Phys.* **52**, 35–53 (1983). doi:10.1016/0021-9991(83)90015-3